High-Temperature Superconductivity And Its Applications

Senior project report submitted in partial fulfillment of the requirements for the degree of

BS in Applied Physics

Under the guidance of

Dr. Walid Malaeb

Lebanese American University

April, 2023

BEIRUT CAMPUS
P.O. Box: 13-5053 Chouran
Beirut 1102 2801
Lebanon
Tel: +961 1 786 456
+961 3 791 314
Fax: +961 1 867 098

BYBLOS CAMPUS
P.O. Box: 36
Byblos
Lebanon
Tel: +961 9 547 262
+961 3 791 314
Fax: +961 9 546 262

NEW YORK HEADQUARTERS & ACADEMIC CENTER
211 East 46th Street
New York, NY 10017-2935
United States
Tel: +1 212 203 4333
Fax: +1 212 784 6597

www.lau.edu.lb

High-Temperature Superconductivity And Its Applications

Charles Malik, Khaled Dandan, Rida Younes

Abstract

Discovered over a hundred years ago, superconductivity has revolutionized physics by opening a new door of understanding. Relying on the newly established theories of quantum mechanics to explain the mechanisms and reasons behind conventional and unconventional superconductors alike, superconductivity has sparked a wide interest in physicists in the pursuit of the holy grail of superconductivity: a room temperature and pressure superconductor capable of revolutionizing energy transport and more. This study takes a close look at the origins of superconductivity, the theories behind it and the findings that the cutting edge research being done on copper oxides and iron pnictides has unearthed. The final section of this study analyzes real data, namely resistivity and magnetization, obtained from the iron pnictide $SmFeAsO_{1-x}F_x$.

Table Of Contents

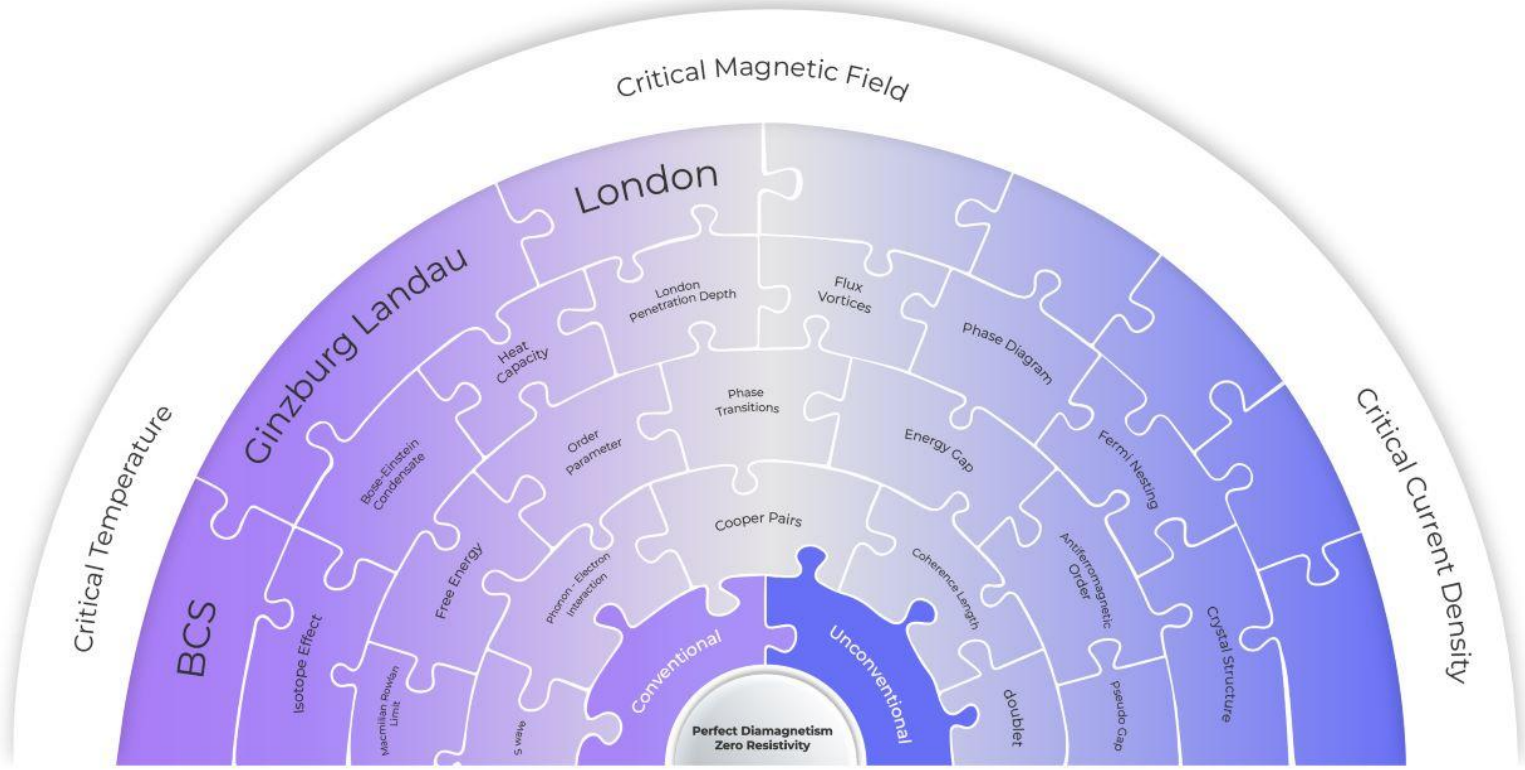

This is a custom map of superconductivity as the subject is understood by the authors.

1. Introduction

We begin our senior study with a historical review and a timeline of superconductivity. Its first discovery was in 1911 with mercury; however, the prerequisite for this discovery came in 1908 when Heike Kamerlingh Onnes was able to liquify helium at 4.5 K [1]. He recorded the phenomenon of zero resistivity in his first experiment.

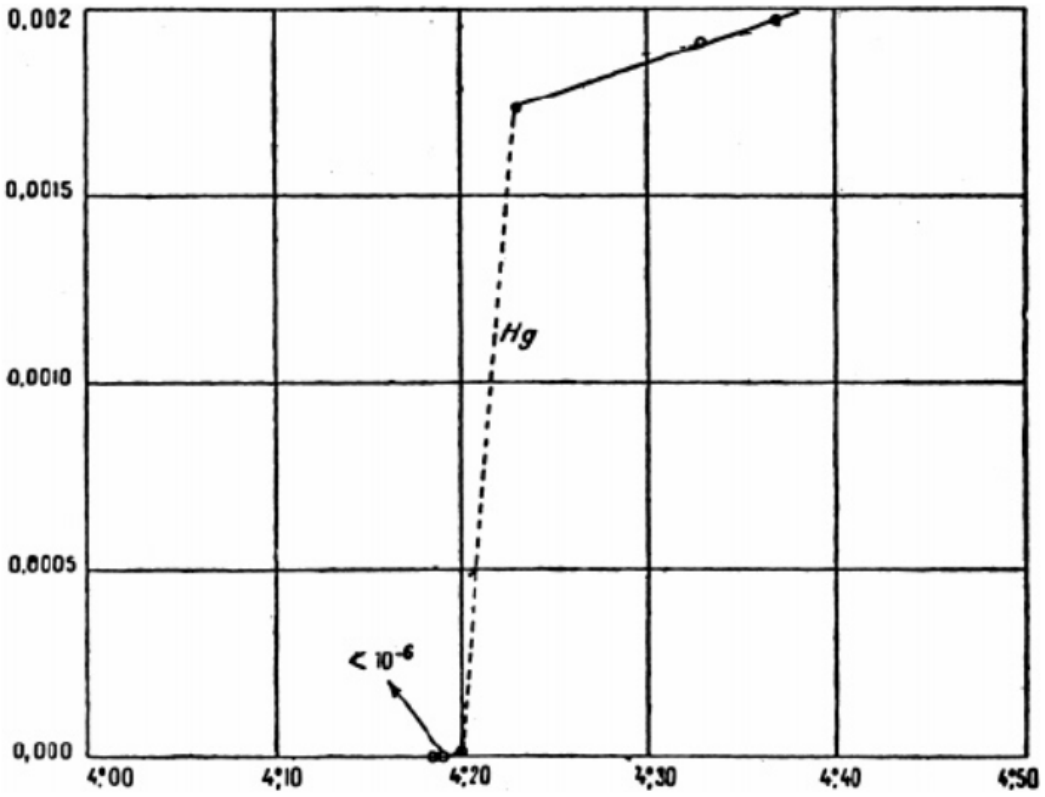

Fig 1 [2]. Onnes's original plot detailing mercury's abrupt resistivity drop as a function of temperature

After that, a formal definition of superconductivity is given: when a material enters its superconducting phase (which occurs below a critical temperature, magnetic field strength, and electric current density denoted by T_c, B_c, and J_c, respectively), it acts like a perfect diamagnet and exhibits zero resistance to electric current. Classical (as opposed to high-temperature)

superconductors are classified into two categories: Type 1 and Type 2 superconductors. Type 1 superconductors have a clear separation between their superconducting and non-superconducting phases. The two factors that can destroy superconductivity are high temperatures above the critical temperature and a strong external magnetic field applied to the superconductor. Type 2 superconductors do not have a fixed separation between their superconducting phase and non-superconducting phase. Instead, they have a mixed phase in between where they act as both normal conductors and superconductors simultaneously. We note that for Type 2 superconductors, there is only one critical temperature (same with Type 1 superconductors), T_c, but they have two critical magnetic fields, B_{c1} and B_{c2}. For any magnetic field strength below B_{c1}, the superconductor is in its superconducting phase. For a field strength between B_{C1} and B_{C2}, we have the mixed phase, and for a field strength greater than B_{C2}, we have the normal phase of conduction. As aforementioned, resistivity (ρ) being 0 is not the only fundamental characteristic of a superconductor. The fundamental proof that superconductivity occurs in a given material, apart from zero resistivity, is the demonstration of the Meissner-Ochsenfeld effect. We examine the first property of superconductors, namely perfect diamagnetism, by diving into the Meissner Effect, which states that a superconductor will always expel a weakly externally applied magnetic field so long as it is below the critical magnetic field threshold. First, the distinction between perfect conductors and superconductors is important to understand. The former is a very good conductor but cannot superconduct; like gold for example, whereas a superconductor exhibits different characteristics that we will discuss shortly. If initially the superconductor is not in its superconducting phase and no external magnetic field is applied, we can expect that after cooling the material to below T_c, the superconductor will completely expel the applied magnetic

field. If the same case is taken, but instead of having no externally applied magnetic field before cooling and then a field is applied, it is observed that after cooling that field is also expelled. The former case is called zero field cooled because there was no initial magnetic field applied before cooling, while the latter case is called field cooled, meaning that there was an externally applied field before cooling. In either case, the magnetic field is totally expelled out of the superconductor. Taking the case of the perfect conductor, we also examine both cases of field cooling and zero field cooling. In the zero-field-cooled case of a perfect conductor, after cooling, there is no magnetic field observed, just like with superconductors. The difference arises in the field-cooled case, where after cooling, magnetic flux changes are observed in the perfect conductor.

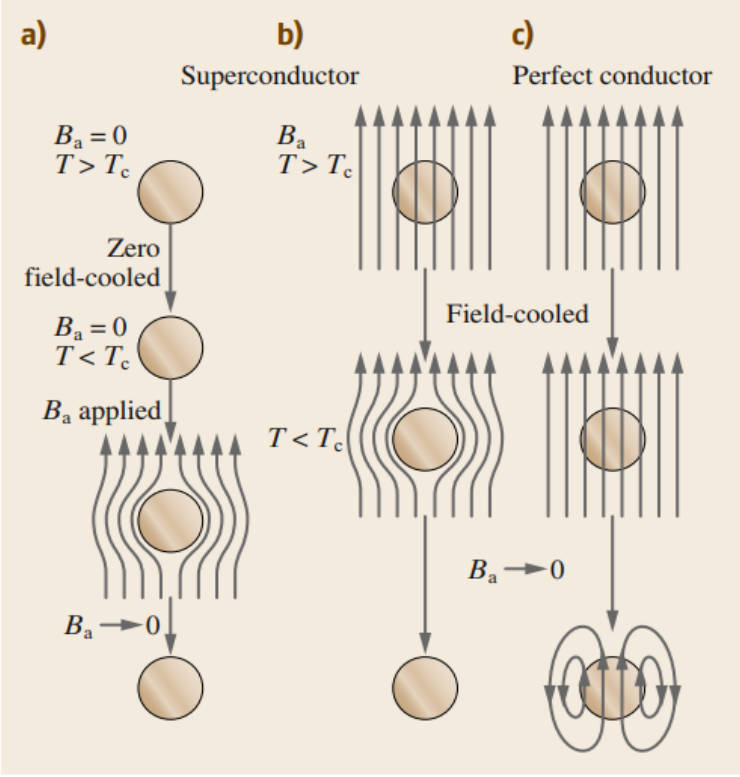

Fig 2 [3]. Behavior of magnetic field lines in zero field cooled and field cooled superconductors versus their behavior in a perfect conductor

So the conclusion is that superconductors expel any externally applied magnetic field when cooled down, regardless of whether the field was applied before or after cooling, whereas perfect conductors preserve some sort of magnetic field variations in the case where the magnetic field is applied before cooling. Even though superconductors expel magnetic fields, there is still some penetration of the field into the material. This penetration decays exponentially as the distance traveled into the material increases.

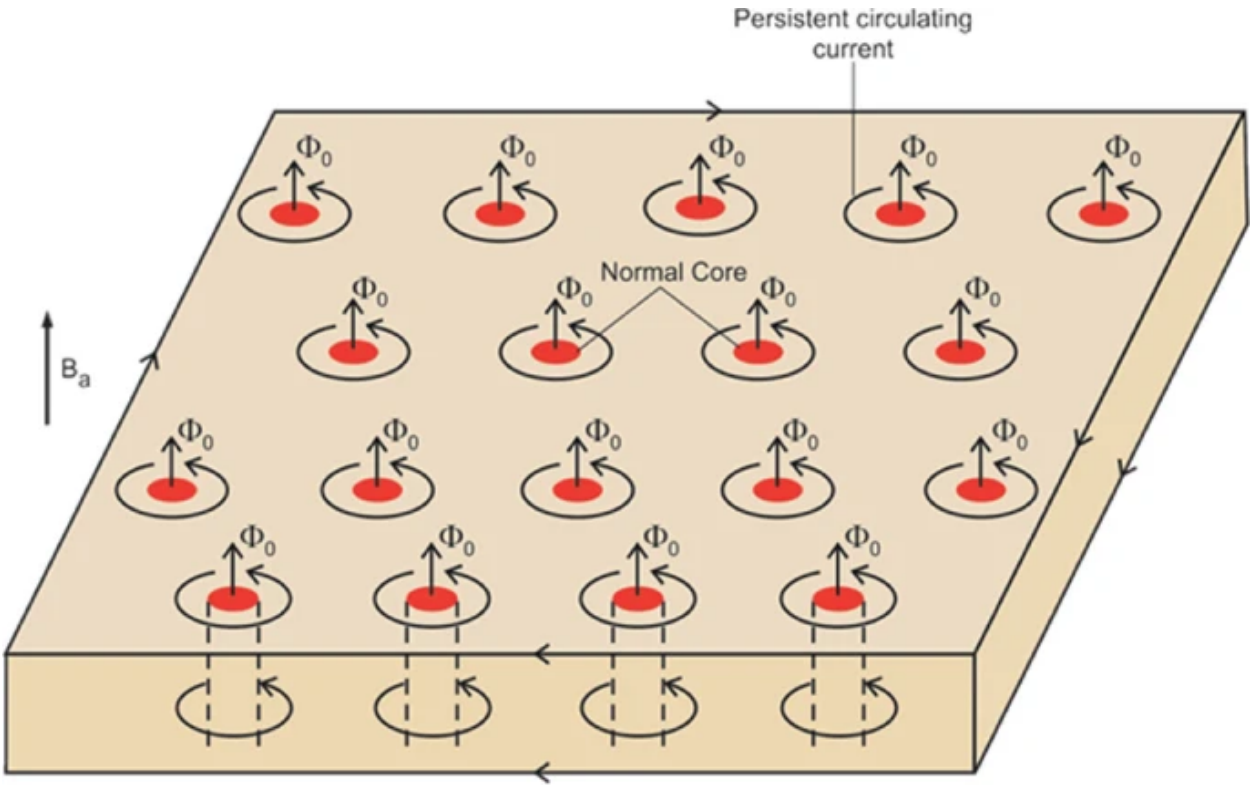

Fig 3 [4]. Flux vortices in type 2 superconductors

This explains why we have a mixed phase in Type 2 superconductors. The mixed phase arises from flux vortices on the surface of the superconductor that penetrate the material and create an area of normal conduction and lock the superconductor in place when hovering over a

magnet; however, if the total material is considered, we can still say that the material is superconducting. Also, these flux vortices are in motion and move on the surface of the material rather than being static points of normal conduction. [5]

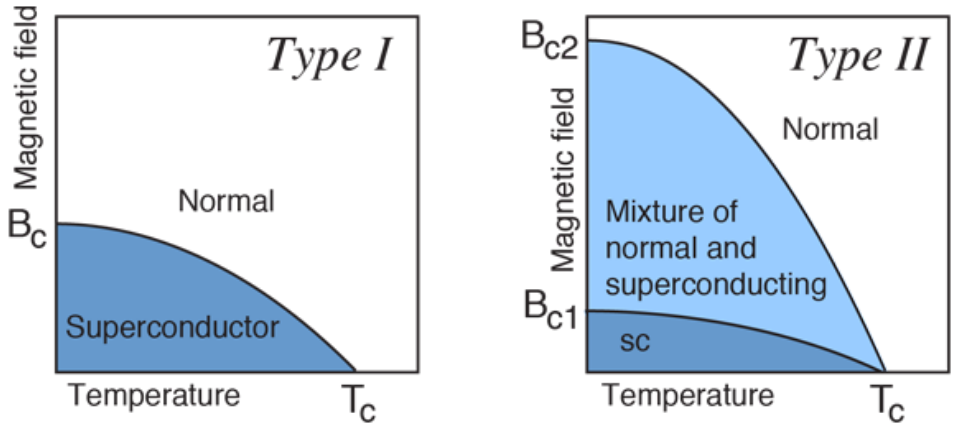

Fig 4 [6]. Phase diagram for Type 1 and Type 2 superconductors

2. Theoretical Background

a. London's Equations

London's theory describes a maximum penetration depth and mathematically predicts Meissner's effect. The first London equation states that $\frac{\partial j_s}{\partial t} = n_s e^2(\frac{E}{m})$, where j_s is the superconducting current density and n_s is the density of cooper pairs in the superconductor, while the second London equation says that $\nabla \times j_s = - n_s e^2(\frac{B}{m})$. Applying $\nabla \times B = \mu_0 J$, then we get $\nabla^2 \times B = \frac{B}{\lambda_s^2}$,where $\lambda_S = \sqrt{\frac{m}{(\mu_0 n_s e^2)}}$ is the London penetration depth, which is a measure of how far the magnetic field can penetrate the superconductor. Knowing that $\nabla \times E = - \frac{\partial B}{\partial t}$ and

substituting it in the second London equation, we get, $\frac{\partial}{\partial t}[(\frac{m}{n_s e^2} \times \nabla \times j_s) + B] = 0$ which shows that the flux created by the currents is equal to the flux created by the external magnetic fields, thus achieving a screening of the external magnetic field and mathematically proving Meissner's effect.

b. Ginzburg-Landau Theory

Ginzburg and Landau were also among the first to tackle the issue of superconductivity with what is known as the Ginzburg-Landau (GL) theory, which was first developed to describe phase transitions. Since the transition from the normal to the superconducting state is a phase transition, it can be used to describe superconductivity. In GL theory there exists the concept of an order parameter, which is a measure of how ordered the new system is and which we will denote as ψ. Above the phase transition temperature (T_c), $\Psi = 0$ while below it $\Psi \neq 0$. Thus, the actual free energy expansion becomes $F = F_n + \alpha\Psi^2 + \boldsymbol{\beta}\Psi^4 + \ldots$, where F is the total free energy, F_n is the total free energy of the normal state, and α and **β** are coefficients, where $\alpha = A(T - T_C)$ (A is a non-zero coefficient), and **β** is also temperature dependent. For the purposes of this study, we shall only consider up to the fourth power of ψ. Below the transition temperature, any ordered phase that develops in the system is an equilibrium phase, which is defined by the minimization of the free energy $[\frac{\partial F}{\partial \Psi} = 0]$. After differentiating F with respect to ψ and equating that to 0 to find the minima and substituting the roots of the equation back into the original one, we obtain $F = F_n - \frac{A^2(T-T_C)^2}{2\boldsymbol{\beta}}$ [7]. Having discussed the general GL theory, it is time to turn our attention to applying it on a superconductor. Here, $\Psi = \Psi_0 e^{i\Phi}$,where Ψ_0 is the

amplitude, ϕ is the superconducting phase, and $\Psi_0 = |n_s|$, where n_s is the density of cooper pairs.

The free energy of a superconductor is given by

$$F_s = F_n + Condensation\,energy + Kinetic\,energy + Field\,Energy$$

Substituting into the equation, we obtain

$$F_{GL} = F_n + \int d^3r[\alpha|\Psi^2| + \frac{\beta}{2}|\Psi^4| + \frac{1}{2m^*}|(-i\hbar\nabla - \frac{e^*A}{c})\Psi|^2] + (\nabla x A^2)/8\pi] .$$

Differentiating this expression with respect to Ψ, Ψ^*, and A and manipulating the resulting equations yields the standard GL equations of superconductivity, which are:

1) $\alpha\Psi + \boldsymbol{\beta}|\Psi|^2\Psi + (1/2m^*)(-i\hbar\nabla - (e^*A)/c)^2\Psi = 0$. where m^*=2m and e^*=2e

2) $J_s = ((e^*\hbar)/(2m^*i))(\Psi^*\nabla\Psi - \Psi^*\nabla\Psi^*) - (e^{*2}|\Psi|^2A)/(cm^*)$ [8]

An important parameter to note in the GL theory is the Ginzburg-Landau parameter, defined as κ = λ/ε , where ε, as we will later show, is the coherence length of the cooper pair. When κ is less than 1/√2 , the material is a type 1 superconductor; otherwise, it's a type 2 superconductor.

The GL theory has several limitations, like not considering the effects of interactions between electrons, which can be important in high-temperature superconductors, and only describing the behavior of the order parameter and not other properties of the system such as entropy, heat capacity, etc.

c. BCS Theory

In 1957, John Bardeen, Leon Cooper, and John Schrieffer developed the BCS theory, which was the first successful quantum mechanical theory of superconductivity. The theory is based on the idea that at very low temperatures, electrons in a material can pair up and move

through the material without resistance. The theory proposes that at low temperatures, the electrons can interact with each other through vibrations in the material's lattice. These vibrations, called phonons, cause the electrons to attract each other, forming what is known as Cooper pairs.

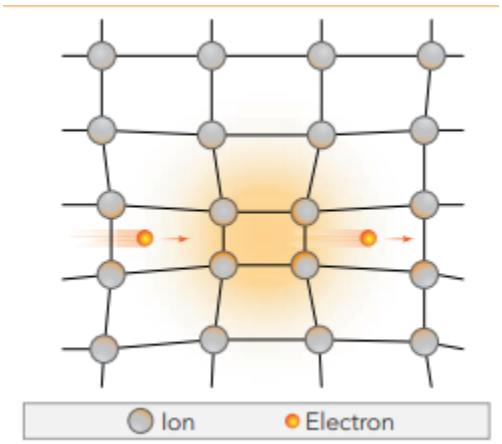

Fig 5 [9]. Lattice deformation and Cooper pair formation

Cooper pairs have unique properties that allow them to move through the material without resistance. Cooper pairs bind together by an attractive force that arises from the exchange of phonons, which are vibrations in the crystal lattice of the material. This pairing is a quantum mechanical effect that occurs only at low temperatures. In addition, the pairing of Cooper pairs results in a total spin of zero. This means that the pair is in a spin-singlet state and is not affected by magnetic fields. Because magnetic fields can cause electrons to scatter and lose energy, the zero spin property of Cooper pairs helps them move through the material with very little resistance. Also, Cooper pairs are typically much larger than individual electrons, since the attractive force between the electrons is spread out over a large region of the crystal lattice, causing the electrons to move in a coordinated way. The length of the Cooper pair, i.e the distance after which the Cooper pair breaks, is known as the coherence length, and is denoted by

ε. Lastly, Cooper pairs have a finite lifetime, which is related to the energy gap that forms in superconductors. At low temperatures, the energy gap prevents individual electrons from moving through the material but allows Cooper pairs to move freely. [9,10]

The lattice vibrations supply the electrons with an energy of the order of ħwd. This explains why only electrons near the fermi surface participate in superconductivity, since electrons occupying states well below the fermi surface, when supplied with an energy of ħwd, would have to jump to an occupied state, which is impossible. Thus, only electrons occupying states with an energy difference of less than ħwd between them and the fermi surface's energy can participate in superconductivity, and they can only reach states with a maximum of ħwd above the fermi surface energy. Electrons in that special region form cooper pairs, and no single electron states exist there anymore, creating the aforementioned energy gap in the density of states of the order of $2\hbar w_d$. [5]

Any arbitrarily weak potential is enough to cause cooper pairing, since this potential will cause a minimization in the energy of the 2 electron state, now given by: $E = 2E_f - 2\hbar w_d e^{\frac{-2}{v_0 g(E_f)}}$ where $g(E_F)$ is the density of states at the fermi level, E_f is the energy of the fermi level, and V_o is the arbitrarily weak potential. Using second quantization and the anti-commutation laws, Bardeen, Cooper, and Schrieffer showed that the BCS hamiltonian is given by $H = 2\Sigma k \varepsilon k c k\uparrow$, where $-V_o$ is the BCS potential, ck↑† and c−k↓† are the creation operators for a particle with momentum k↑ and −k↓ respectively, and c−k'↓ and ck'↑ are the annihilation operators for a particle with momentum −k'↓ and k'↑ respectively.

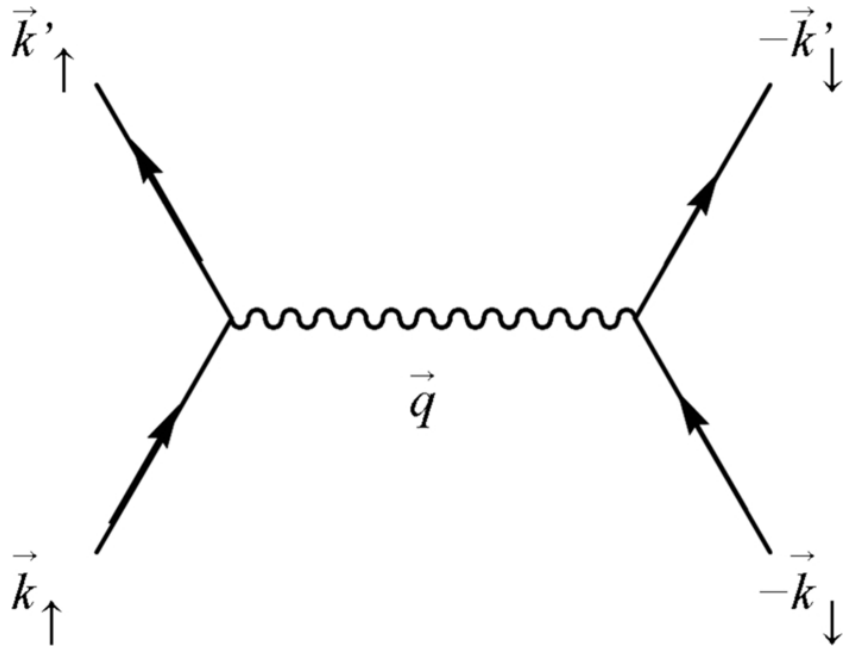

Fig 6 [11]. Feynman diagram depicting the pairing of two electrons with opposite spins and momenta

These represent the scattering of the 2 electrons initially at k'↑ and -k'↓, one from a lower to a higher energy to a lower energy state and the other from a lower to a higher energy state. From there, they then showed that the energy is expressed as $2\Sigma(\varepsilon_k|v_k|^2) + \Sigma(V_{kk'}v_k^* u_k v_{k'} u_{k'}^*)$, where $|v_k|^2$ is the probability that the 2 electron state characterized by $(k\uparrow, k\downarrow)$ is occupied and $|u_k|^2$ that that state is empty, and $V_{kk'} = -V_0$ is the BCS potential. They simplified this equation further to show that the energy gap is $\Delta = 2\hbar w_d e^{\frac{-2}{v_0 g(E_F)}}$, which is what the binding energy for 2 electrons is for any arbitrarily weak potential (as shown previously). Numerically, it is given by $\Delta = 1.76kT_C$,where k is Boltzmann's constant, and T_c is the critical temperature at which the material becomes a superconductor [5,12,13]. This formula applies to conventional

superconductors. When one supplies an energy greater than the binding energy, the cooper pair separates, and the above formula relates the size of the gap to the thermal energy required to break it.

The predictions that the theory offered were experimentally proven numerous times, some of which were mentioned above like zero resistance and the meissner effect. Other such experimentally proven predictions are:

- The Isotope Effect:

If electrical conduction in mercury were purely electronic, there should be no dependence upon the nuclear masses. However, experiments have shown that there's a dependance of T_c on isotopic mass. The reason for this effect is that when a phonon is created in the lattice, it can be absorbed by an electron, which then moves through the lattice with no resistance. However, the mass of the ions in the lattice can affect the energy of the phonons and their interactions with the electrons. An increase in mass leads to a smaller debye frequency, which in turn yields smaller values of T_c. This dependence of the critical temperature for superconductivity upon isotopic mass was the first direct evidence for interaction between the electrons and the lattice. This supported the BCS theory of lattice coupling of electron pairs. [14]

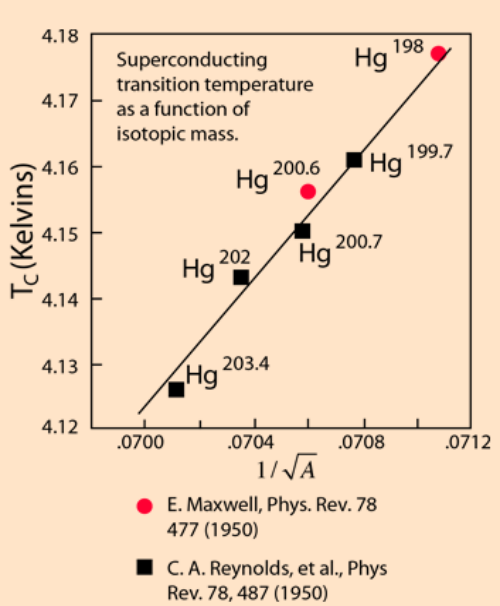

Fig 7 [6]. Plot of T_c versus different isotopes of mercury showing a clear linear relationship between T_c and isotopic mass

- Energy Gap:

The reduction of the energy gap as you approach the critical temperature can be taken as an indication that the charge carriers have some sort of collective nature. That is, the charge carriers must consist of at least two things which are bound together, and the binding energy is weakening as you approach the critical temperature. Above the critical temperature, such collections do not exist, and normal resistivity prevails. This evidence, along with the isotope effect, which showed that the crystal lattice was involved, helped paint the picture of paired

electrons bound together by phonon interactions with the lattice [14].

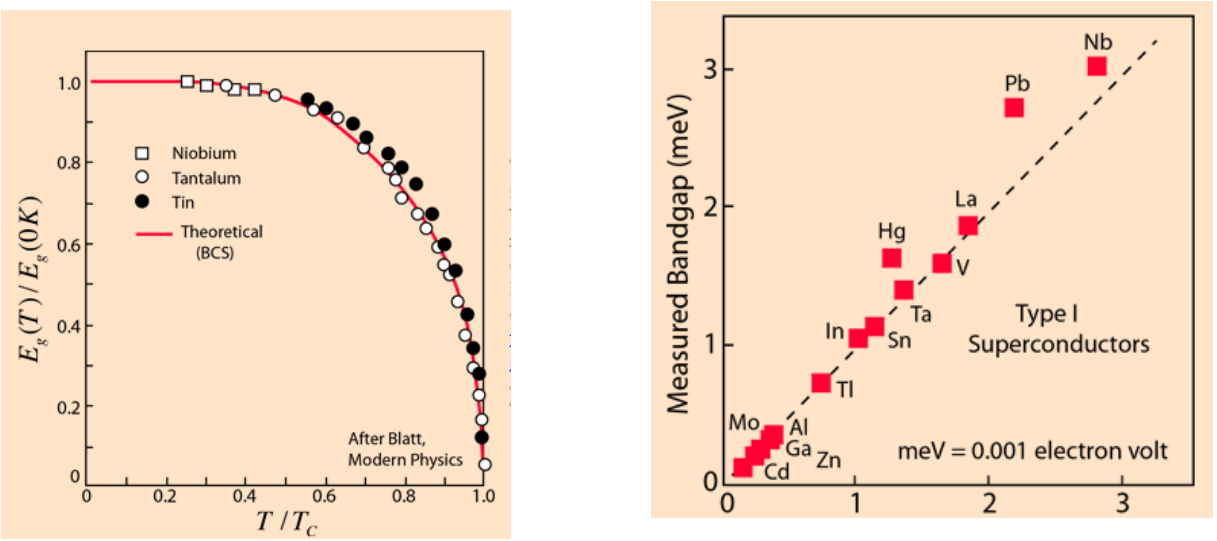

Fig 8(a),(b) [6]. Comparison between BCS theory predictions and experimental observations of band gap strength and the behavior of the band gap with increasing temperature

- Heat capacity:

The vanadium heat capacity experiment showed that superconducting vanadium is very different from vanadium kept in the normal state by imposing a magnetic field on the sample. The exponential increase in the heat capacity of the superconducting vanadium near T_c suggests an abrupt change in the density of states when the material transitions from the superconducting state to the normal state. This exponential increase suggests an energy gap which must be bridged by thermal energy.

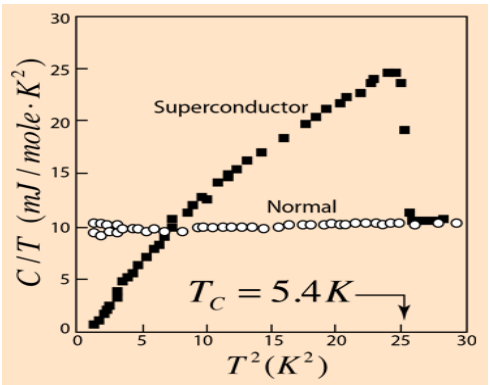

Fig 9 [6]. Experimental data proving a phase transition occurs at Tc

- BCS T_c upper limit :

The Macmillan Rowlan limit describes the maximum temperature at which superconductivity can exist, and it is, as aforementioned, related to the lattice's debye frequency . The relationship is:

$$T_{Cmax} \approx \frac{\boldsymbol{\theta D}}{1.45} \times e^{-1.04(\frac{1+\lambda}{\lambda-\boldsymbol{\delta}})},$$

where θD is the Debye temperature (a measure of the average frequency of the phonons in the material), λ is the dimensionless electron-phonon coupling constant, and δ is a parameter that accounts for the effects of the electronic band structure.

The key factor limiting T_c in this equation is the exponential term, which depends on the ratio of the electron-phonon coupling strength to the phonon frequency. As the frequency of the phonons increases, this ratio becomes smaller and the exponential term becomes larger, leading to a decrease in T_c.

For most conventional superconductors, the Debye temperature is typically around 400 K, which sets an upper limit of around 40 K for T_c based on the McMillan-Rowell limit.

However, unconventional superconductivity is a different phenomenon altogether. Superconductivity isn't formed according to the BCS model [phonon-electron interactions aren't alone in forming the Cooper pairs, and superconductivity in these materials can be exhibited at above 40 K (the maximum temperature that can be theoretically reached according to the BCS theory)]. [15]

3. High-Temperature Superconductors

a. Introduction to High T_c Superconductors

After stating theories, we then define what a high-temperature superconductor is. These compounds are called high T_c superconductors because they can exhibit their superconducting state, meaning perfect diamagnetism and zero resistivity, above a temperature of 77K, which is the boiling point of liquid nitrogen, a coolant significantly cheaper than liquid helium. Prior to the discovery of these compounds, liquid helium was the only coolant able to reach sufficiently low temperatures for the emergence of superconductivity. Moreover, the superconducting mechanism for these compounds can't be explained by the BCS theory, which has additionally earned them the name of unconventional superconductors [16]. Also, it was predicted by the BCS theory that the maximum critical temperature that a superconductor can reach while still existing in its superconducting phase is 40K. High T_c superconductors exceed this limit, marking a shift into newer, previously undiscovered physics.

b. Types of High Tc Superconductors

i. Cuprates

The first type of high-T_c superconductor to be discovered was the copper oxide superconductor, also known as cuprates. Cuprates are complex compounds characterized by layers of CuO planes and require doping in order to exhibit superconductivity, as we shall discuss later on in this chapter. The first discovery of cuprate superconductivity was in 1986, when Bednorz and Muller discovered in Ba-doped La_2CuO_4 that the current density affects the temperature dependence of the conductivity in the transition region from the normal to the superconducting state, which they declared might point to high T_c superconductivity. Later in the same year, Tanaka, Kitazawa,

Uchida, and Takagi confirmed that the transition temperature for that compound was 30 K. In February of 1987, Chu et al. reported a transition temperature of above 90K in $YBa_2Cu_3O_7$, which ignited a fervor in the scientific community. [16]

ii. Iron Pnictides

Iron pnictides are compounds containing iron and a pnictide (a group 15 element), and they too require doping in order to exhibit superconductivity. Superconductivity in iron pnictides was first discovered by Hideo Hosono et al. in 2006 in LaFePO with a transition temperature of approximately 4K. Subsequently, superconductivity was found in 2007 in LaNiAsO with a transition temperature of 2.4K and in 2008 in $LaFeAsO_{1-x}F_x$ with a transition temperature of 26K. [17]

c. Crystal Structure

i. Cuprates

The crystal structure of copper oxides consists of crystallized, layered, two-dimensional planes of CuO_2 with antiferromagnetically aligned spins. The material therefore has a net magnetic moment of zero because the magnetic moments of the neighboring spins cancel one another out. This antiferromagnetism, as we shall shortly discuss, is imperative in the formation of superconductivity in these materials. The crystal-layered planes also have room for doping, which is the controlled addition or subtraction of impurities [18]. These extra spaces are called interstitials, which are where the doping occurs. The level of doping plays a crucial role in the analysis of the phase diagram, which we will discuss later.

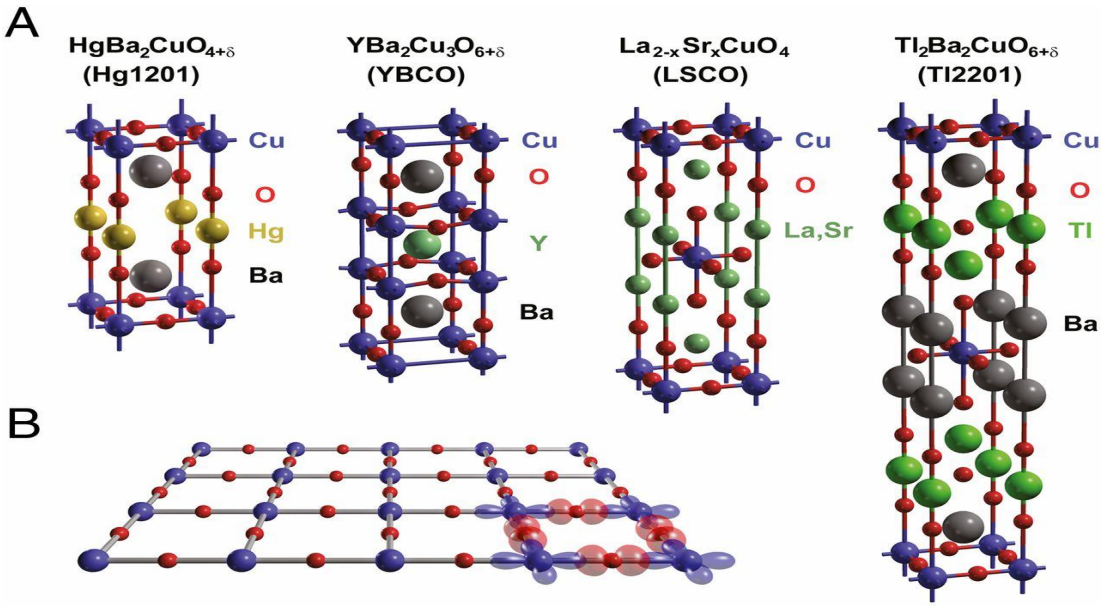

Fig 10 [18]. Cuprate Superconductor crystal structure

ii. Iron Pnictides

The crystal structure of the pnictides, however, is completely different. Iron pnictides are generally described as superconductors containing at least iron and a pnictide (an element in group 15 of the periodic table) organized in multiple three-dimensional layers. However, iron pnictides are subcategorized into many different families, each having a unique crystal structure. Here are some of the most notable subclasses and their key differences:

1111: The 1111 subclass of iron pnictide superconductors contains one iron atom and one pnictide atom per unit cell. The crystal structure of 1111 compounds is tetragonal, and perhaps the most well-known 1111 compound in this family is LaFeAsO, whose unit cell contains 2 molecules and whose chemical formula is ($La_2O_2Fe_2As_2$). $La_2O_2Fe_2As$ has a T_c of around 26 K [Fig. a] [19-20]

122: The 122 subclass of iron pnictide superconductors contains one iron atom and two pnictide atoms per unit cell. The crystal structure of 122 compounds is orthorhombic, with each unit cell having eight formula units. The most well-known 122 compound is $BaFe_2As_2$, which has a T_c of around 38 K. Fig.b. [20- 21]

111: The 111 subclass of iron pnictide superconductors contains one iron atom and one pnictide atom per unit cell, similar to the 1111 subclass. However, the crystal structure of 111 compounds is hexagonal, with each unit cell having two formula units. The most well-known 111 compound is LiFeAs, which has a T_c of around 18 K. [Fig.c.] [20-22]

11: The 11 subclass of iron pnictide superconductors contains one iron atom and one pnictide atom per unit cell, similar to the 111 and 1111 subclasses. However, the crystal structure of 11 compounds is simple and monoclinic, with each unit cell having two formula units. The best-known 11-compound is FeSe, which has a T_c of around 8 K. These different subclasses of iron pnictide superconductors have different crystal structures, which affect their electronic and magnetic properties. For example, the 122 subclass tends to have stronger electron correlations than the 1111 subclass, which can lead to different types of superconductivity. Additionally, the doping behavior of each subclass can vary, with some being more sensitive to doping than others. [Fig.d] [20-23]

One of the main differences between iron pnictide superconductors and copper oxide superconductors is their crystal structure. Copper oxide superconductors have a layered crystal structure, with the superconducting properties arising from the two-dimensional copper-oxide planes. In contrast, iron pnictide superconductors have a more complex crystal structure, with the

superconducting properties arising from the interaction between multiple layers of iron and pnictide atoms.

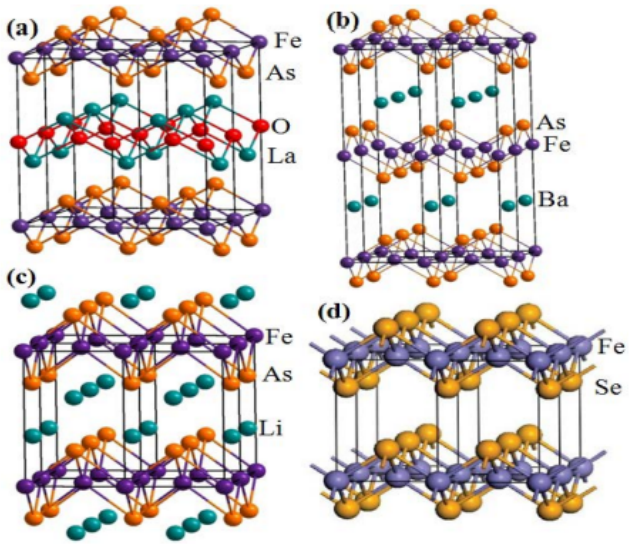

Four families of iron-based superconductors, (a) 1111, (b) 122, (c) 111, (d) 11 types

Fig 11 [20]. Different structures of the iron pnictide family

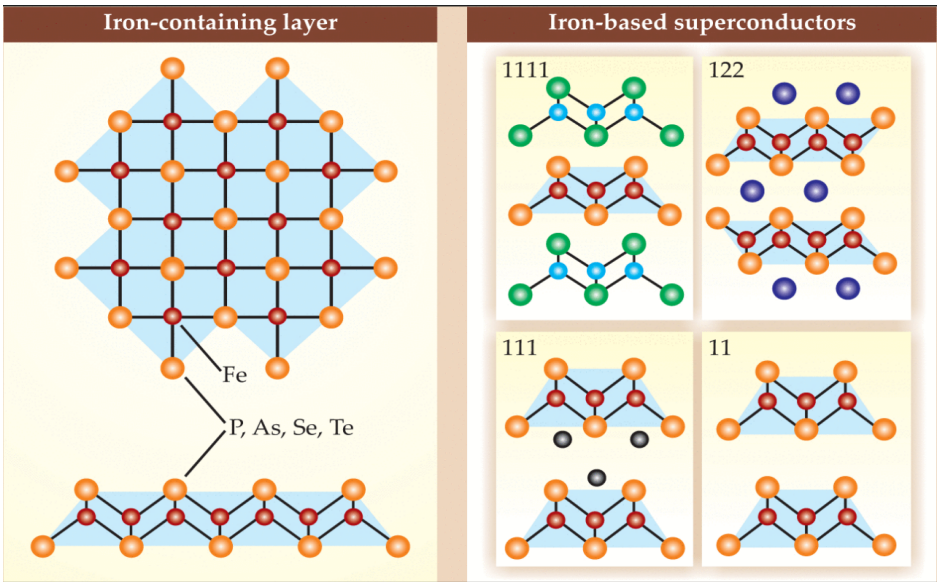

Fig 12 [24]. Iron pnictide layers

d. Phase Diagrams

i. Cuprates

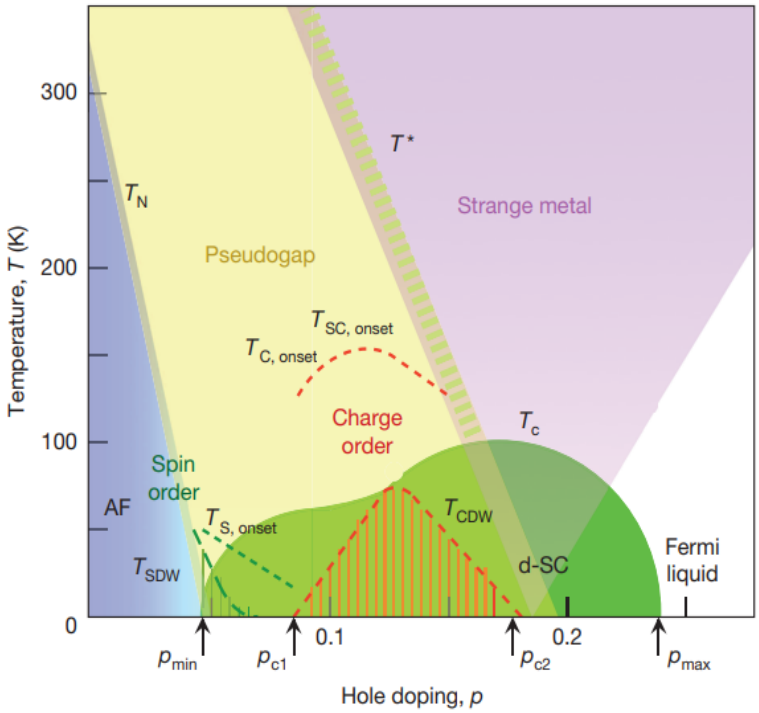

Fig 13 [25]. Typical phase diagram for high T_c superconductors

The phase diagram for cuprates is studied by noting the different regions, phase transitions, and d-order parameter changes , ranging from the antiferromagnetic phase to the superconducting dome and more. The x-axis represents the level of hole doping, which is also referred to as P doping, while the y-axis represents the temperature of the superconductor. Between the origin and P minimum, the copper oxide superconductor is characterized by its antiferromagnetic order. This is true between some high temperatures and the temperature slowly marking a change in the ordered parameter from the antiferromagnetic to the pseudogap region. This means that above this temperature, the superconductor is in its antiferromagnetic state and is not capable of superconducting. Once the temperature is reached, the pseudogap region

appears. It is characterized by a reduction in the density of states as well as the early formation of cooper pairs. This second feature is notable because it was originally thought that Cooper pairs only form at low temperatures, which turned out to be true for conventional superconductors, but not for high-temperature superconductors. These newly formed cooper pairs are unstable and have a short coherence length due to perturbations that prevent the superconducting phase from beginning; however, they allow for the pseudogap region to appear under a high temperature called T^*. After further increasing the temperature and doping level, the superconductor enters its superconducting phase, which on the phase diagram is in a dome shape. This phase is characterized by the classic features of superconductivity, namely zero resistivity and perfect diamagnetism. Another major phase is the strange metal phase, where superconductivity is destroyed and new properties appear. The strange metal phase is characterized by several unusual properties that distinguish it from ordinary metals. One of the most striking features is the linear dependence of electrical resistivity on temperature, which is in contrast to the quadratic dependence observed in normal metals. This means that as the temperature increases, the resistivity of the material increases linearly, indicating a breakdown of the usual Fermi liquid behavior. In addition, the strange metal phase is also characterized by non-Fermi liquid behavior, such as a violation of the so-called Luttinger theorem and a breakdown of the Landau quasiparticle picture. The origin of the strange metal phase is still not fully understood, but it is believed to be related to the complex interplay between electronic interactions, disorder, and fluctuations in the system. In particular, it has been suggested that the strange metal phase may be related to the presence of quantum critical points, which are special points in the phase diagram of a material where the behavior undergoes a dramatic change. [25]

ii. Iron Pnictides

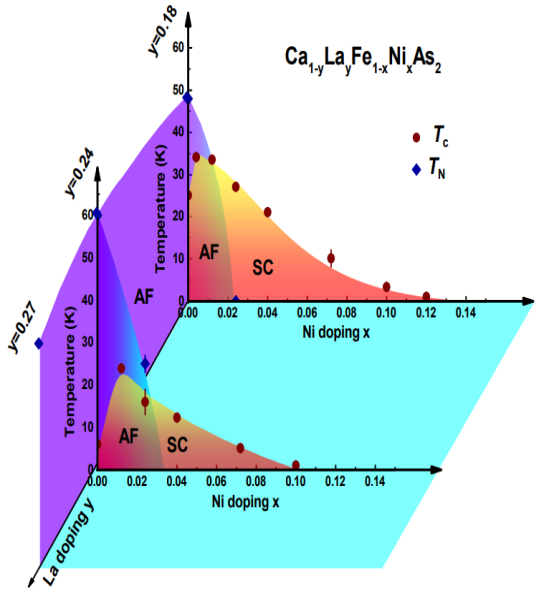

Fig 14 [26]. Phase diagram for $Ca_{1-y}La_yFe_{1-x}Ni_xAs_2$

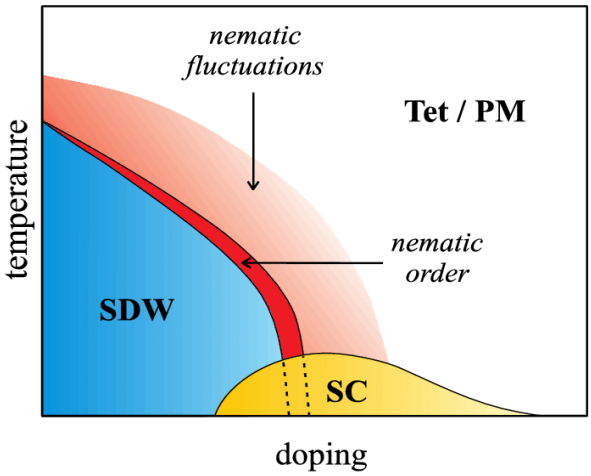

Fig. 15 [27]. Another phase diagram for iron pnictides, Quantum In Complex Matter 2013, Antonio Bianconi

The phase diagram for some iron pnictides is similar to that of cuprates in that the parent compound must exhibit an antiferromagnetic order that is slowly destroyed. However, unlike the cuprates, the superconducting dome can coexist with the antiferromagnetic order for some

doping levels. Moreover, both isovalent doping (replacing atoms with others having an equal number of valence electrons) and charge carrier doping (hole or electron doping), as opposed to uniquely charge carrier doping in cuprates, are effective in the establishment of superconductivity in iron pnictides. In some cases, the antiferromagnetic order parameter is closely accompanied by changes in the nematic order along with nematic fluctuations (a fluctuation in the orientation of the particles due to thermal energy), where the nematic order consists in the spontaneous breaking of the electronic symmetry between the x and y directions in the Fe-plane but not of the underlying lattice. In some iron pnictides, however, a spin density wave (SDW) region (a region with the periodic alignment of the electrons' spins) can coexist with or completely replace the antiferromagnetic region. [28-29]

e. Mechanism of Superconductivity

i. Cuprates

According to the most popular explanation, known as the resonating valence bond (RVB) theory, the high-temperature superconductivity of copper oxides results from the pairing of electrons through the exchange of bosonic excitations, such as spin or charge fluctuations (variations in the material's magnetic moment and charge density respectively). The RVB theory states that the copper oxides' highly correlated electrons result in the production of singlet pairs, which can then condense into a superconducting state. Although there is still much to learn about the precise nature of the bosonic excitations that mediate the pairing of electrons in copper oxides, it is believed that the doped holes in the copper oxide lattice play a significant role. As

these doped holes interact with the copper oxide lattice's electrons, a superconducting state is created. [30]

ii. Iron Pnictides

Several theories have been put forth regarding the method by which iron pnictides superconduct. One of the most popular hypotheses is based on the idea of "nesting" between various Fermi surface regions, which is the surface that divides the material's occupied and unoccupied states. While cuprates have a single Fermi surface sheet, in in iron pnictides, nesting between various Fermi surface regions causes magnetic fluctuations to occur, which later act as a mediator in the pairing of electrons. A superconducting state is created as a result of electron pairing. The interaction between superconductivity and magnetism is a crucial aspect of iron pnictide superconductivity. Magnetic ordering in iron pnictides happens at a temperature greater than the superconducting transition point, which distinguishes them from other materials. Although it is yet unclear how superconductivity and magnetism interact in iron pnictides, this interaction is expected to be crucial in determining the characteristics of the superconducting state. Also, there is evidence that the pairing of electrons in iron pnictides is influenced in part by the existence of spin fluctuations.[31]

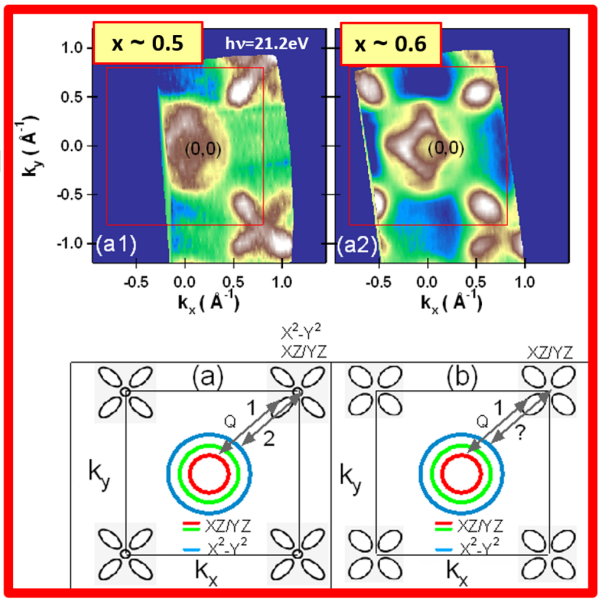

Fig 16 [32]. Experimental data and its respective schematic on the Fermi surface sheets in an iron pnictide

f. Superconducting Gap Symmetry

i. Cuprates

Cuprates exhibit d-wave pairing symmetry, meaning the wave function of the Cooper pair moving along the x-axis has a positive sign while the one moving along the y-axis has a negative sign [33]. This effect is argued to be universal for all cuprate-based superconductors. [34]

ii. Iron Pnictides

For the iron pnictides, we need to introduce the idea of p-wave superconductivity/triplet superconductivity/ odd parity superconductivity. It is characterized by any compound that has its angular momentum quantum number S=1, with the allowed values for spin therefore being m_s= -1, 0, 1 hence triplet. In fact, iron pnictides exhibit p-wave pairing. This is done by analyzing the temperature dependence of the superfluid density,

$$\rho_s(T) = \frac{1}{\lambda^2(T)}$$

where λ is the London penetration depth.

We have two cases of p wave pairing, one where the vector potential (A) is parallel to the gap axis (l), and the other where (A) is perpendicular to (l). However, Knight shift (a relative shift in the nuclear magnetic resonance frequency for atoms in a metal compared with the same atoms that are in a non-metallic environment) experiments showed that p-wave pairing should be prohibited. Note that Knight shift consideration in superconductors started in the early 1960s, when it was believed that ferromagnetism is antagonistic to superconductivity. However, a simple extrapolation of theoretical results in regards to the Knight shift obtained for classical BCS superconductors probably is not valid for the newly discovered class of iron-based superconductors. Also, p-wave superconductivity can be uniquely determined from the temperature dependence of the polar A⊥l case of $\rho_s(T)$, and thus the lack of experimental studies for confidently detecting p-wave pairing is related not just to the fabrication of samples but also to choosing an experimental technique for which the polar A⊥l orientation can be studied. The case considered was with A⊥l. $J_c = (ln(\kappa) + 0.5) + \rho_s^{1.5}(T)$

, where $\boldsymbol{\kappa} = \frac{\lambda}{\xi}$ is the Ginzburg-Landau parameter.

Analysis of self-field critical current data and superfluid density data obtained on a wide variety of iron-based superconductors using p-wave models finds superconducting parameters that are more consistent under a p-wave model compared with the generally accepted s-wave model. Also, observation of the polar A⊥l model in both the self-field critical current data and superfluid density data strongly indicates the existence of p-wave pairing in the iron pnictides. [35]

g. Room Temperature Superconductors

Close to and at room temperature, superconductors have been theoretically and experimentally verified, which means that they can be used practically as long as cooling isn't an issue. Unfortunately, room-temperature superconductors come at a cost of high pressures (reaching 500 GPa), making their applicability in everyday life much more difficult. Researchers have achieved ever higher transition temperatures, such as 164 K under 31 GPa in the $HgBa_2Ca_2Cu_3O_{8+\delta}$ (Hg1223) cuprate high-temperature superconductor (HTS) in 1994 by Chu et al. and 203 K under 155 GPa in the H_3S hydride in 2015 by Eremets et al.. After successfully synthesizing hydrides inside a diamond anvil cell (DAC) through laser heating, a T_c up to 260 K was obtained by Hemley et al. in LaH10 under 180–200 GPa in 2019. Most recently, Dias et al. achieved a T_c of 287 K under 267 GPa in a C-S-H, which is the highest T_c ever recorded. A T_c of 287 K is very close to 300 K, which is loosely assigned as room temperature [36]. However, we need to keep in mind that for a superconductor to work efficiently, it must be well below its critical temperature, meaning that if we needed a superconductor to operate at temperatures close to 300K, we would need a material with a T_c of $\approx$ 450K.

h. Applications

There are several potential applications for high-temperature superconductors currently being investigated. Superconducting generators are a major potential application. It offers better system stability than conventional generators and is able to operate at higher magnetic fields. Also, this generator is more efficient, meaning it can save more fuel, covering the capital costs of the generator. Its requirements, however, are quite difficult to reach, making the idea of a

superconducting generator out of reach for the moment. Other applications include power transmission lines. Conventional power lines are limited when it comes to current capacity, due to heat dissipation issues and impedance problems. Superconducting power lines, on the other hand, offer a higher current capacity because there is no impedance. So in theory a superconducting cable can carry an infinite current with low voltage. On average, 4 percent of power is lost due to current impedance in conventional wires. This loss will be eliminated by the use of superconducting power lines. This is why there is a huge interest in the iron pnictide family of high-temperature superconductors because they are more malleable than copper oxides, which are brittle, meaning they can be used in fashioning power lines. Finally, a large potential area of application is in the medical field. There are already superconductors being used in the medical field, most notably in the MRI (medical resonance imaging) machine. The superconductors in use are conventional superconductors (albeit ones with a high B_c) that require very low temperatures to operate and thus need a cold environment (which ramps up costs). In this regard, high-temperature superconductors offer a lucrative solution. Other areas of application include communication systems, MAGLEV trains, digital devices, and magnetic energy storage units. [37]

4. Results and Discussion

Resistivity

i. Experimental Data

In order to analyze and interpret resistivity data, we should introduce the concept of the four-point probe method. This is a technique that was first introduced by Frank

Wenner over 100 years ago in 1915 to accurately measure resistance, and subsequently, resistivity. The problem with measuring resistance with only two probes that allow a current to flow through one probe into the material and out the other probe is that this is an inaccurate technique. The measurement intrinsically includes the contact resistance R_c at the probes' position, which is in series with the resistance of the material. The basic idea of the 4P probe method is to measure the voltage drop between the two inner probes while a current passes through the two outer probes. However this concept changes a lot when considering different geometries, materials (isotropic vs anisotropic, bulk vs. thin films), and spacing between the probes. The simplest cases of an isotropic semi-infinite 3D bulk and an infinite 2D sheet are considered first. Four probes are placed collinearly, with equal spacing between adjacent probes. The current injected from one of the outer probes is assumed to spread spherically in the material. In the case of a semi-infinite 3D bulk material, its resistivity is given by:

$$\rho_{3D}^{line} = 2\pi s \frac{V}{I}$$

In the case where the thickness (t) of the material is much smaller than the spacing between the probes (s), we can consider this a 2D infinite sheet. The main difference is that in this case, the current spreads cylindrically, not spherically, in the material. This affects the expression of the current density and hence the resistivity, which is given by:

$$\rho_{2D}^{line} = \frac{\pi t}{ln2} \frac{V}{I}$$

Sometimes, instead of arranging the probes in a straight line, they are arranged in a square configuration. The advantage to this setup is that the area is reduced because the

maximum distance between two probes is $\sqrt{2s}$ instead of 3s. It is clear that the measured resistance R does not depend on the spacing of the probes in the case of the infinite 2D sheet, whereas in the 3D case, resistance R decreases with increasing probe spacing. This result is somewhat shocking seeing that as distance increases the resistance is decreasing. This is because in a 2D sheet, the resistance is directly compensated by moving in a perpendicular direction to the probes, so there is no dependence on spacing, whereas in a 3D material, there is an overcompensation for the resistance by spreading into the material, which causes this inverse relationship between distance and resistance. Usually, for macroscopic 4P probe setups, the separation between the probes is in the millimeter range, which is comparable to the dimensions of the material being probed. [38]

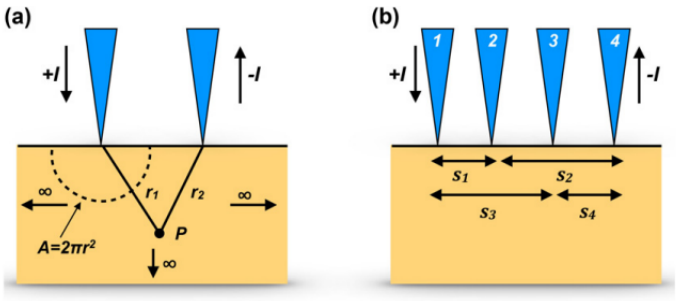

Fig 17 [38]. Schematics of (a) a two-point probe and (b) a collinear 4P probe array with equidistant contact spacing

s4

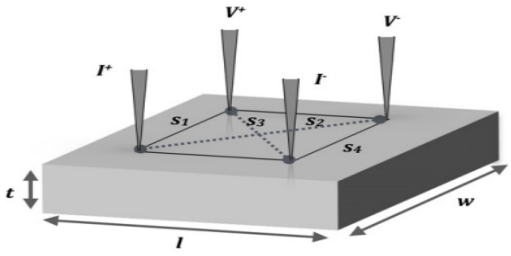

Fig 18 [38]. Schematic of a square 4P probe configuration with s1 = = s and s2 = s3 = √2s.

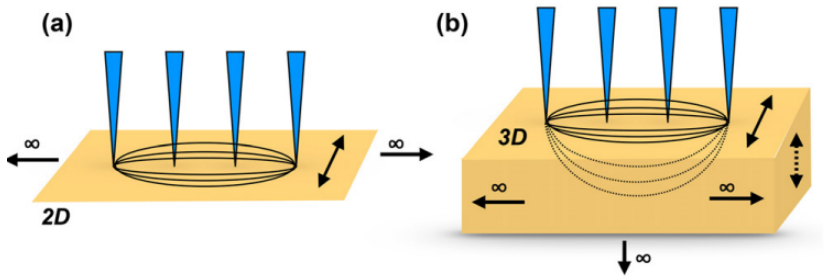

Fig 19 [38]. Diagrams of the current flow pattern in (a) an infinite 2D sheet and (b) a semi-infinite 3D material.

ii. Results

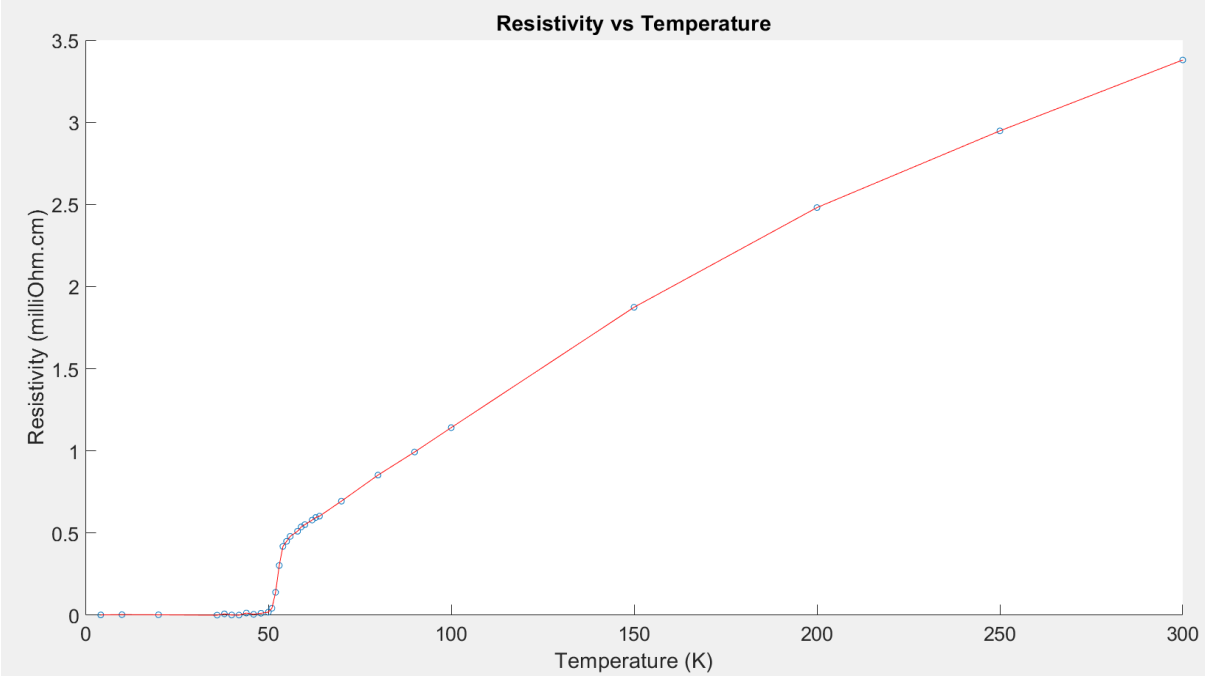

Fig 20. Raw data plotted. Resistivity measured in (milliOhm.cm) vs Temperature measured in (K). (**Appendix 1)**

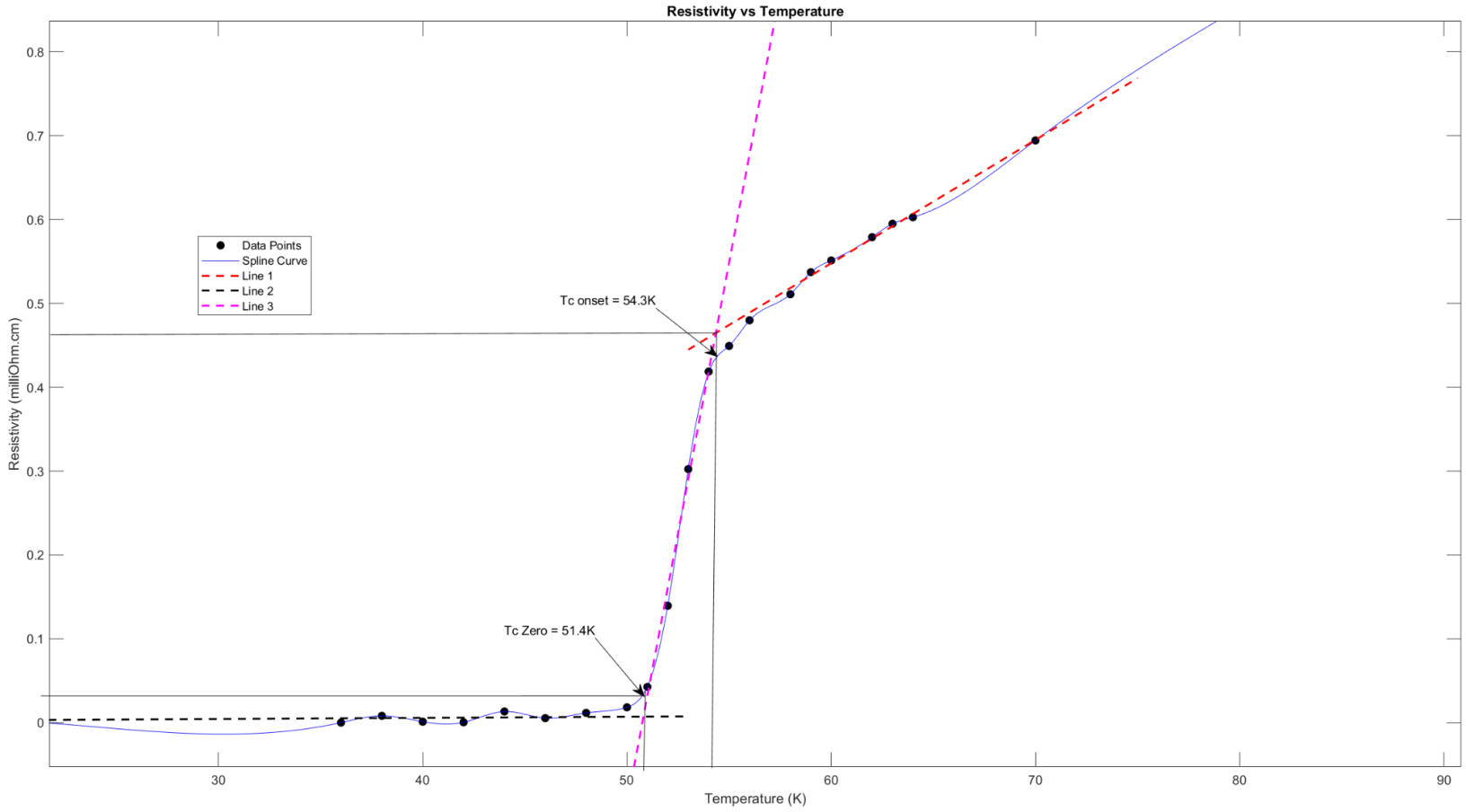

Fig 21. Zoomed in version of the initial plot indicating different critical temperatures. (**Appendix 2)**

We need first to define the different types of critical temperatures that can be extracted from the resistivity vs. temperature graph. In our data's case, there is only one doping level, so there can't be comparisons of the different types of critical temperatures and whether those temperatures increase with increased doping levels (or vice versa); however, it is still possible to extract these temperatures directly from the graphs.

a) T_c^{onset} is regarded as the cross point of the fitting lines for resistivity in the normal state near transition and in the drop area during the transition. $T_c^{onset} = 54.3K$

b) T_c^{zero} is also regarded as the cross point of the line for zero resistivity and the ρ –T curve. $T_c^{zero} = 51.4K$

It is also useful for us to plot the derivative of resistivity with respect to temperature. The width of the peak indicates how much T_c^{onset} and T_c^{zero} are far apart. The width is taken at half its maximum.

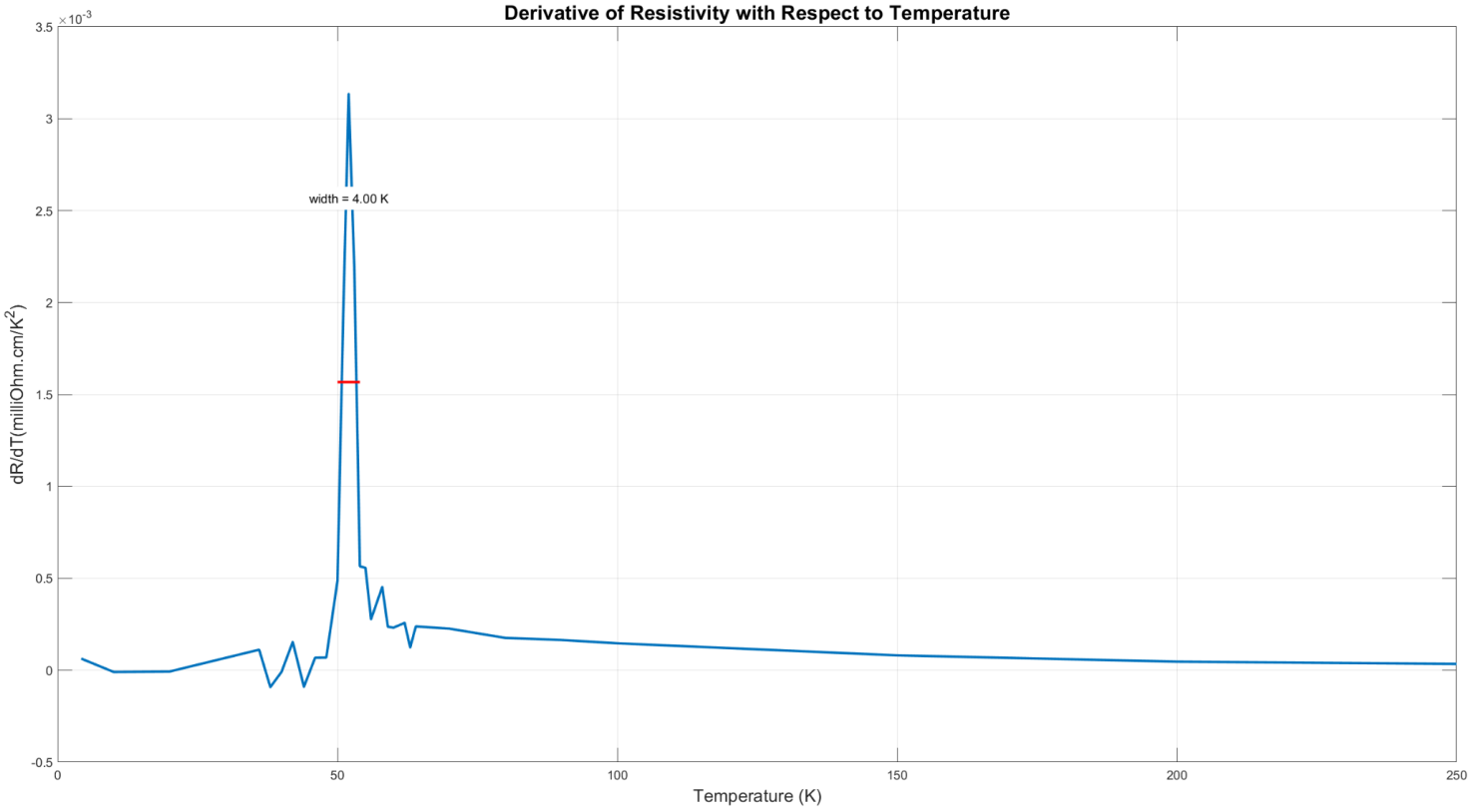

Fig 22. The derivative of resistivity with respect to temperature. The width at half maximum is 4K, as calculated by code indicated by the red line. (**Appendix 3)**

As for the residual resistivity, it was calculated purely through MATLAB (**Appendix 4)**, by the extrapolation method, where a linear extrapolation of the data before the onset of superconductivity intersects the y-axis. The final result is $\rho_0 = 0.060688\ milliOhm.cm$.

All the values of the critical temperatures are summarized in the following table (according to our data):

$T_c = \frac{Tc\ onset + Tc\ zero}{2}$	T_c^{onset}	T_c^{zero}	$\Delta T_c = T_c^{onset} - T_c^{zero}$
52.85K	54.3K	51.4K	2.9K

Fig 23. Summarized data extracted from plots.

x	T_c^{onset} (K)	T_c^{zero} (K)	T_c^{anom} (K)
0	—	—	147.1
0.02	—	—	145.2
0.04	—	—	144.7
0.06	—	—	129.5
0.08	7.6	—	—
0.1	39.1	30.31	—
0.12	54	49.7	—
0.14	55.9	51.3	—
0.16	57.4	53.7	—
0.18	57.6	53.5	—
0.2	57.7	53.3	—
0.22	57.8	52.9	—
0.24	58	52.7	—
0.26	58.1	52.2	—
0.28	57.7	50.9	—
0.3	57.9	51.2	

Fig24 [39]. Different critical temperatures for the same compound at different doping levels obtained from literature.

It is important to compare our results with those found in literature. The doping level targeted in our data analysis is 0.14. This resulted in T_c^{onset} = 54.3K and T_c^{zero} = 51.4K are shown in **Fig23.** We can see that these results match up closely with those in **Fig24** which has at a doping level of 0.14 a T_c^{onset} = 55.9K and T_c^{zero} = 51.3K. This is further confirmation in the accuracy of our data and its analysis.

iii. Discussion

The above data allowed us to gain information about the sample's critical temperatures from the plot of the resistivity versus temperature. Also, it is worth noting that typically before measuring resistivity, an XRD investigation takes place so that the crystallographic planes and different peaks are known. The idea behind this is to know the maximum intensity peaks at different doping levels. Without knowing the different doping levels, it isn't possible to draw the phase diagram. For our data, however, the temperature variations are fully understood. The fact that the residual resistivity is very small as well as the fact that the drop in resistance to 0 is a sharp drop rather than a gradual decrease tells us that the sample is a good pure sample. This demonstrates that Sm-1111 is a good homogeneous superconductor with few impurities that would hinder this effect.

Magnetization

i. Experimental Data

The magnetic property measurement system (MPMS) is an extremely sensitive magnetometer capable of detecting magnetic fields of strength down to 10^{-18} T. The main artifact used in the MPMS is the Superconducting Quantum Interference Device (SQUID). The SQUID operates based on the phenomena of the Josephson junction and magnetic flux quantization. A ring of superconducting wire is shaped, with a Josephson junction at the top and bottom of the loop. Josephson junctions can carry current up to a critical value Ic without registering voltage; as such, a current of value $I = 2I_c$ is made to flow through the ring; I_c flows

through the upper part while I_c flows through the lower part. We pass the sample through a superconducting coil to establish a phase difference between the two junctions (the induced current flows opposite to the existing current in one half while it flows with the existing current in the other half). The total current fluctuates in proportion to the magnetic flux (where the magnetic flux quantum is $\boldsymbol{\phi}_0 = \frac{e}{\pi\hbar}$; as such when the total flux is a half integer multiple of the magnetic flux quantum, I is at its minimum, while I is at its maximum at integer multiples of the magnetic flux quantum. The current is extremely sensitive to any small changes in the flux, and as such, so is the voltage. The voltage oscillates with respect to the magnetic flux, where when the magnetic flux is an integer multiple of the magnetic flux quantum, it's at its minimum, while it's at its maximum when the magnetic flux is a half-integer multiple of the magnetic flux. Therefore, measuring the voltage allows us to sense small changes in the current, flux, and ultimately, the magnetic field. [40]

Fig 25 [41]. MPMS Quantum design

ii. Results

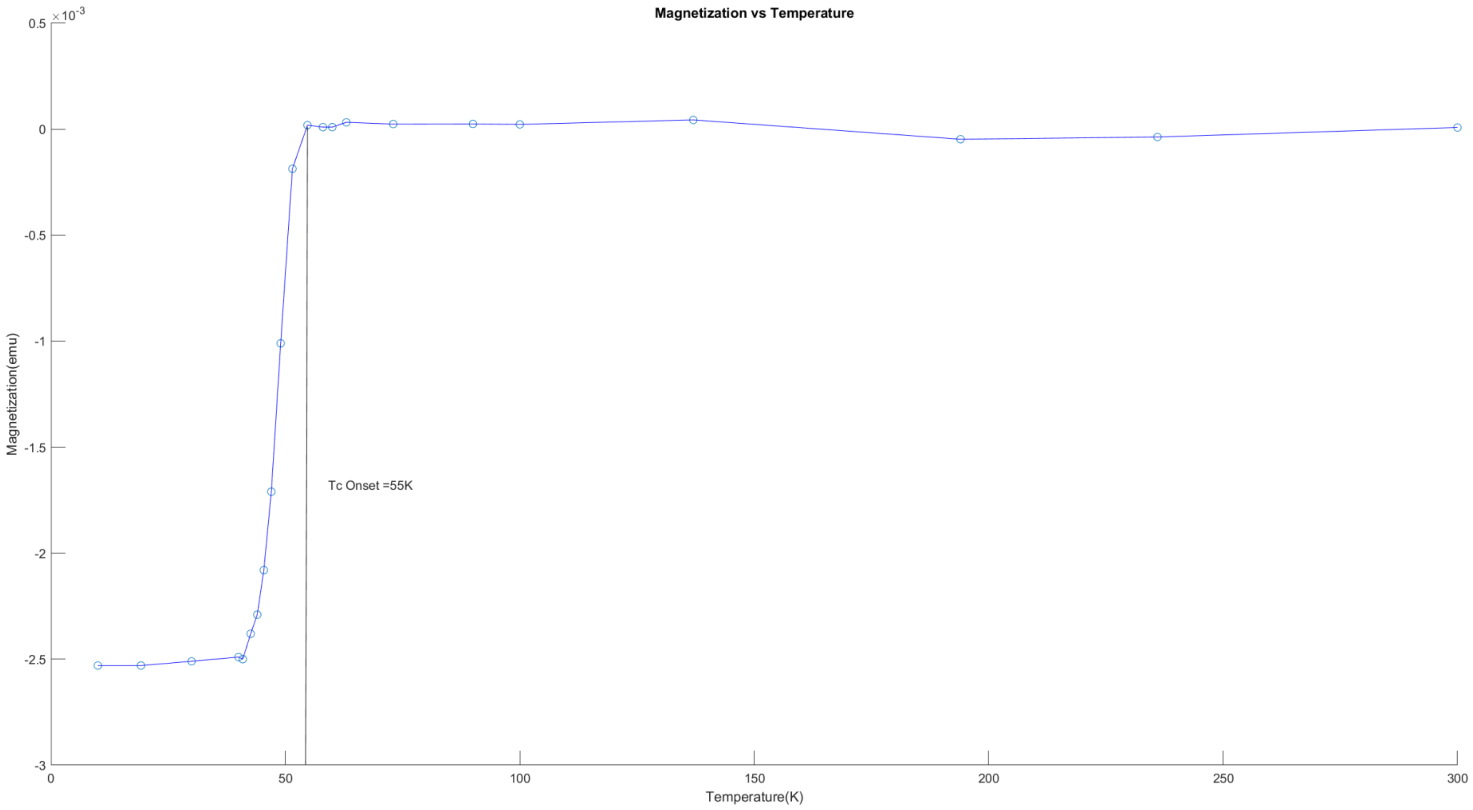

Fig 26. Raw data plotted. Magnetism measured in (emu) vs Temperature measured in (K). **(Appendix 5)**

We can draw many conclusions from the long moment vs temperature's plot. We realize a sharp drop in the magnetic moment just after T_c was reached (51K), after which the magnetic moment stabilizes and remains constant at -2.5 emu with a slight deviation downward with decreasing temperature.

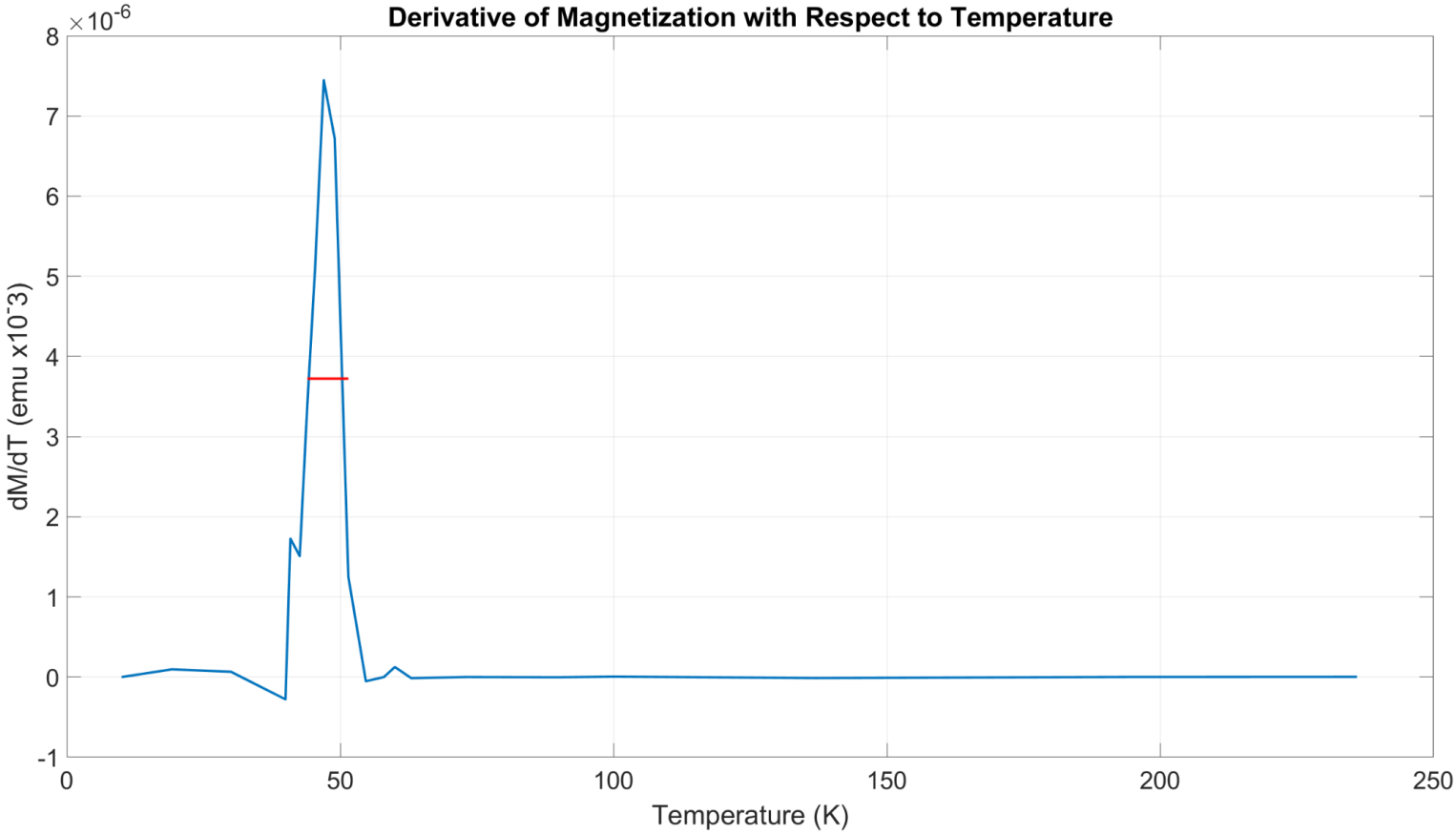

Fig 27. The derivative of magnetism with respect to temperature. The width at half maximum is 4K, as calculated by code indicated by the red line. **(Appendix 6)**

From plotting the slope of the derivative of the magnetization with respect to temperature vs temperature, we observe with more precision where the drop in the magnetic field occurred and when it stops fluctuation. A stop in fluctuation indicates we've reached our maximum magnetic field generated. We can also determine ΔT_c which tells us how sharp the drop was.

a) We note from the plot that T_c^{onset} is approximately 55K which represents the peak of the plot for slope.

b) T_c^{zero} is shown to be around 47 K

All the values of the critical temperatures are summarized in the following table:

$T_c = \frac{Tc\ onset + Tc\ zero}{2}$	T_c^{onset}	T_c^{zero}
51K	55K	47K

Fig 28. Summarized data extracted from plots.

iii. Discussion

The sharp drop in the magnetic moment implies that the sample was zero field-cooled (ZFC), since in field-cooled (FC) methods, the curve would show a wider transition width as the external magnetic field "soothes" the drop. The stabilization of the magnetic moment represents the upper critical field, where if that value is exceeded by imposing an external magnetic field the superconducting state is destroyed. The slight increase in magnetic moment strength after T_c can be interpreted as impurities. While the value of T_c for this material to have zero resistivity is 55K, the drop of magnetic field occurs at $T_c^{onset} = 54$K, which indicates that in order to observe perfect diamagnetism we need first to observe a drop in resistivity.

Lastly we observe that the magnetic moment produced by the sample is very weak, which can limit its applications, as its critical current density would be weak as well.

Note that all these experimental data were taken by W. Malaeb et al at Keio University - Japan and provided to us for the sake of demonstration.

Appendix

1:

```
T = [4.2, 10, 20, 36, 38, 40, 42, 44, 46, 48, 50, 51, 52, 53, 54, 55, 56, 58, 59, 60,
62, 63, 64, 70, 80, 90, 100, 150, 200, 250, 300];
resistivity = [0.00177432, 0.00331207, 0.00236576, 0.000118288, 0.00816187,
0.00118288, 0.000473151, 0.0133666, 0.00544124, 0.0117105, 0.0183347, 0.0427021,
0.139462, 0.302463, 0.41874, 0.449258, 0.479895, 0.511005, 0.537265, 0.551223,
0.57902, 0.594989, 0.602796, 0.694351, 0.852739, 0.993384, 1.14148, 1.87428, 2.48098,
2.94786, 3.37937];
% create a scatter plot with red curve
Figure;
hold on;
scatter(T, resistivity);
plot(T, resistivity, 'r');
hold off;
% add labels and title
xlabel('Temperature (K)');
ylabel('Resistivity (milliOhm.cm)');
title('Resistivity vs Temperature');
```

2:

```
% plot the data points with markers
plot(data(:, 1), data(:, 2), 'ko', 'MarkerFaceColor', 'k')
hold on
% interpolate the data points with a spline curve
x_interp = linspace(min(data(:, 1)), max(data(:, 1)), 1000);
```

```
y_interp = interp1(data(:, 1), data(:, 2), x_interp, 'spline');
% plot the curve
plot(x_interp, y_interp, 'b', 'LineWidth', 0.5)
% extend the lines slightly beyond the data points
line1 = data(18:24, :);
line2 = data(1:10, :);
line3 = data(12:15, :);
p1 = polyfit(line1(:, 1), line1(:, 2), 1);
x1 = linspace(line1(1, 1) - 5, line1(end, 1) + 5, 100);
y1 = polyval(p1, x1);
p2 = polyfit(line2(:, 1), line2(:, 2), 1);
x2 = linspace(line2(1, 1) - 5, line2(end, 1) + 5, 100);
y2 = polyval(p2, x2);
p3 = polyfit(line3(:, 1), line3(:, 2), 1);
x3 = linspace(line3(1, 1) - 5, line3(end, 1) + 5, 100);
y3 = polyval(p3, x3);
% plot the lines
plot(x1, y1, 'r--', 'LineWidth', 1.5)
plot(x2, y2, 'k--', 'LineWidth', 1.5)
plot(x3, y3, 'm--', 'LineWidth', 1.5)
% add labels and legend
xlabel('Temperature (K)')
ylabel('Resistivity (milliOhm.cm)')
title('Resistivity vs Temperature')
legend('Data Points', 'Spline Curve', 'Line 1', 'Line 2', 'Line 3')
```

3:

```
% Resistivity data

temperature = [4.2, 10, 20, 36, 38, 40, 42, 44, 46, 48, 50, 51, 52, 53, 54, 55, 56,
58, 59, 60, 62, 63, 64, 70, 80, 90, 100, 150, 200, 250, 300];

resistivity = [0.00177432, 0.00331207, 0.00236576, 0.000118288, 0.00816187,
0.00118288, 0.000473151, 0.0133666, 0.00544124, 0.0117105, 0.0183347, 0.0427021,
0.139462, 0.302463, 0.41874, 0.449258, 0.479895, 0.511005, 0.537265, 0.551223,
0.57902, 0.594989, 0.602796, 0.694351, 0.852739, 0.993384, 1.14148, 1.87428, 2.48098,
2.94786, 3.37937];

% Calculate derivative of resistivity divided by temperature

dRdT = diff(resistivity)./diff(temperature);

dRdT_over_T = dRdT./temperature(1:end-1);

% Find the index and value of the maximum peak

[max_peak, max_peak_index] = max(dRdT_over_T);

% Find the width of the peak by finding the two temperatures where the

% derivative is half of the maximum value

half_peak = max_peak/2;

left_index = find(dRdT_over_T(1:max_peak_index) < half_peak, 1, 'last');

right_index = max_peak_index + find(dRdT_over_T(max_peak_index:end) < half_peak, 1) -
1;

width = temperature(right_index) - temperature(left_index);

% Plot the derivative of resistivity divided by temperature versus temperature

figure;

plot(temperature(1:end-1), dRdT_over_T, 'LineWidth', 2);

hold on;

plot([temperature(left_index), temperature(right_index)], [half_peak, half_peak],
'r', 'LineWidth', 2);

text(temperature(left_index) + width/2, half_peak + 0.001, sprintf('width = %0.2f K',
width), 'HorizontalAlignment', 'center', 'BackgroundColor', 'w');

xlabel('Temperature (K)', 'FontSize', 20);

ylabel('dR/dT(milliOhm.cm/K^2)', 'FontSize', 20);
```

```
title('Derivative of Resistivity with Respect to Temperature', 'FontSize', 25);

set(gca,'fontsize', 20);

grid on;
```

4:

```
% Define the temperature and resistivity arrays

T = [4.2, 10, 20, 36, 38, 40, 42, 44, 46, 48, 50, 51, 52, 53, 54, 55, 56, 58, 59, 60,
62, 63, 64, 70, 80, 90, 100, 150, 200, 250, 300];

R = [0.00177432, 0.00331207, 0.00236576, 0.000118288, 0.00816187, 0.00118288,
0.000473151, 0.0133666, 0.00544124, 0.0117105, 0.0183347, 0.0427021, 0.139462,
0.302463, 0.41874, 0.449258, 0.479895, 0.511005, 0.537265, 0.551223, 0.57902,
0.594989, 0.602796, 0.694351, 0.852739, 0.993384, 1.14148, 1.87428, 2.48098, 2.94786,
3.37937];

% Define the temperature range for the extrapolation

extrapolation_T = [200, 250, 300];

% Find the index of the temperature where the sharp drop in resistivity occurs

sharp_drop_T_index = find(T == 51);

% Take the data points up to the temperature just before the sharp drop in
resistivity

T_for_extrapolation = T(1:sharp_drop_T_index-1);

R_for_extrapolation = R(1:sharp_drop_T_index-1);

% Perform a linear fit on the selected data points

p = polyfit(T_for_extrapolation, R_for_extrapolation, 1);

% Extrapolate the fit to the desired temperature range

extrapolated_R = polyval(p, extrapolation_T);

% Calculate the residual resistivity by taking the y-intercept of the extrapolated
line

residual_resistivity = extrapolated_R(end);

% Display the result

fprintf('The residual resistivity is %f milliOhm.cm.\n', residual_resistivity);
```

5:

```
Temperature=[300,236,194,137,100,90,73,63,60,58,54.7,51.5,49,47,45.4,44,42.6,40.9,40,
30,19.2,10];

Magnetization=[7.85*10^-6,-3.69*10^-5,-4.75*10^-5,4.35*10^-5,2.25*10^-5,2.46*10^-5,2.
39*10^-5,3.22*10^-5,9.56*10^-6,9.51*10^-6,1.89*10^-5,-1.87*10^-4,-1.01*10^-3,-1.71*10
^-3,-2.08*10^-3,-2.29*10^-3,-2.38*10^-3,-2.5*10^(-3),-2.49*10^(-3),-2.51*10^(-3),-2.5
3*10^(-3),-2.5301*10^(-3)];

%create a scatter plot with blue curve

hold on;

scatter (Temperature,Magnetization);

plot(Temperature,Magnetization,'b');

hold off;

%add labels and title

xlabel('Temperature(K)');

ylabel('Magnetization(emu)');

title('Magnetization vs Temperature');
```

6:

```
% Magnetization data

temperature = [10, 19.2, 30, 40, 40.9, 42.6, 44, 45.4, 47, 49, 51.5, 54.7, 58, 60,
63, 73, 90, 100, 137, 194, 236, 300];

magnetization = [-2.53*10^-3, -2.53*10^-3, -2.51*10^-3, -2.49*10^-3, -2.5*10^-3,
-2.38*10^-3, -2.29*10^-3, -2.08*10^-3, -1.71*10^-3, -1.01*10^-3, -1.87*10^-4,
1.89*10^-5, 9.51*10^-6, 9.56*10^-6, 3.22*10^-5, 2.39*10^-5, 2.46*10^-5, 2.25*10^-5,
4.35*10^-5, -4.75*10^-5, -3.69*10^-5, 7.85*10^-6];

% Calculate derivative of magnetization divided by temperature

dMdT = diff(magnetization)./diff(temperature);

dMdT_over_T = dMdT./temperature(1:end-1);

% Find the index and value of the maximum peak

[max_peak, max_peak_index] = max(dMdT_over_T);
```

```
% Find the width of the peak by finding the two temperatures where the

% derivative is half of the maximum value

half_peak = max_peak/2;

left_index = find(dMdT_over_T(1:max_peak_index) < half_peak, 1, 'last');

right_index = max_peak_index + find(dMdT_over_T(max_peak_index:end) < half_peak, 1) -
1;

width = temperature(right_index) - temperature(left_index);

% Plot the derivative of magnetization divided by temperature versus temperature

figure;

plot(temperature(1:end-1), dMdT_over_T, 'LineWidth', 2);

hold on;

plot([temperature(left_index),  temperature(right_index)],  [half_peak,  half_peak],
'r', 'LineWidth', 2);

text(temperature(left_index) + width/2, half_peak + 0.001, sprintf('width = %0.2f K',
width), 'HorizontalAlignment', 'center', 'BackgroundColor', 'w');

xlabel('Temperature (K)', 'FontSize', 20);

ylabel('dM/dT (emu x10^-3)', 'FontSize', 20);

title('Derivative of magnetization with Respect to Temperature', 'FontSize',25);

set(gca,'fontsize',20);

grid on;
```

References

[1]: van Delft, D., & Kes, P. (2010). The discovery of Superconductivity. *Physics Today*, *63*(9), 38–43. https://doi.org/10.1063/1.3490499

[2]: Goodstein, D., & Goodstein, J. (1996). Richard Feynman and the history of Superconductivity. *NATO ASI Series*, 773–791. https://doi.org/10.1007/978-1-4613-1147-8_41

[3]: Wesche, R. (2015). Physical properties of high-temperature superconductors. https://doi.org/10.1002/9781118696644

[4]: Sharma, R. (2021). The Phenomenon of Superconductivity and Type II Superconductors. *Springer Series in Materials Science*, 15–72. https://doi.org/10.1007/978-3-030-75672-7_2

[5]: Annett, J. F. (2013). *Superconductivity, superfluids, and Condensates*. Oxford University Press.

[6]: Rohlf, J. W. (1994). *Modern physics: From alpha to* Z^0. Wiley.

[7]: Goldenfeld, N. (2018). Lectures on phase transitions and the renormalization group. https://doi.org/10.1201/9780429493492

[8]: Beasley, R. (2009). *Notes on the Ginzburg-Landau Theory* [Lecture Notes]. http://www.icmr.ucsb.edu/programs/documents/Beasley.pdf

[9]: Cho, A. (2011). Superconductivity's smorgasbord of insights: A movable feast. *Science*, *332*(6026), 190–192. https://doi.org/10.1126/science.332.6026.190.

[10]: Blundell, S. (2009). *Superconductivity: A very short introduction*. Oxford university press.

[11]: Kar, R., Goswami, T., Paul, B., & Misra, A. (2014). On magnon mediated Cooper pair formation in ferromagnetic superconductors. *AIP Advances*, *4*(8), 087126. https://doi.org/10.1063/1.4893472

[12]: Poole, C. P., Farach, H. A., & Creswick, R. J. (1995). *Superconductivity*. Academic Press.

[13]: Fernandes, R. (n.d). *Lecture Notes: BCS theory of superconductivity* [Lecture Notes]. https://portal.ifi.unicamp.br/images/files/graduacao/aulas-on-line/fen-emerg/lecture_notes_BCS.pdf

[14]: Schrieffer, J. R. (2018). *Theory of superconductivity*. CRC Press

[15]: Xie, S., Stewart, G., Hamlin, J., Hirschfeld, P., & Hennig, R. G. (2019). Functional form of the superconducting critical temperature from machine learning. Physical Review, 100(17). https://doi.org/10.1103/physrevb.100.174513

[16]: Tanaka, S. (2006). High-Temperature Superconductivity. *The Japan Society of Applied Physics*, *45*(12). https://doi.org/10.1143/JJAP.45

[17]: Hosono, H., & Kuroki, K. (2015). Iron-based superconductors: Current status of materials and pairing mechanism. *Physica C: Superconductivity and Its Applications*, *514*, 399–422. https://doi.org/10.1016/j.physc.2015.02.020

[18]:Michaela-Souliou, S. (2014). *High Pressure Study of High-Temperature Superconductors* [Phd Dissertation]. Max-Planck-Institut für Festkörperforschung Stuttgart.

[19]: Kamihara, Y., Watanabe, T., Hirano, M., & Hosono, H. (2008). ChemInform Abstract: Iron-Based Layered Superconductor La[O1-xFx]FeAs (x = 0.05-0.12) with Tc= 26 K. *ChemInform*. https://doi.org/10.1002/chin.200825008

[20]: Biswal, G., & Mohanta, K. L. (2021a). A recent review on iron-based superconductor. *Materials Today: Proceedings*, *35*, 207–215. https://doi.org/10.1016/j.matpr.2020.04.503

[21]: Rotter, M., Pangerl, M., Tegel, M., & Johrendt, D. (2008). Superconductivity and Crystal Structures of $(Ba_{1-x}K_x)Fe_2As_2$(x=0-1). *Angewandte Chemie*, *47*(41), 7949–7952. https://doi.org/10.1002/anie.200803641

[22]: Pitcher, M. J., Parker, D. R., Adamson, P. C., Herkelrath, S. J. C., Boothroyd, A. T., Ibberson, R. M., Brunelli, M., & Clarke, S. (2008). Structure and superconductivity of LiFeAs. *Chemical Communications*, *45*, 5918. https://doi.org/10.1039/b813153h

[23]: Hsu, F. C., Luo, J. Y., Yeh, K., Chen, T., Huang, T. W., Wu, P. M., Lee, Y., Huang, Y., Chu, Y., Yan, D., & Wu, M. (2008). Superconductivity in the PbO-type structure α-FeSe. *Proceedings of the National Academy of Sciences of the United States of America*, *105*(38), 14262–14264. https://doi.org/10.1073/pnas.0807325105

[24]: Day, C. (2009, July 31). *Iron-based superconductors*. Physics Today; AIP Publishing. https://doi.org/10.1063/1.3206093

[25]: Keimer, B., Kivelson, S. A., Norman, M. R., Uchida, S., & Zaanen, J. (2015). From quantum matter to high-temperature superconductivity in copper oxides. *Nature*, *518*(7538), 179–186. https://doi.org/10.1038/nature14165

[26]: Xie, T., Gong, D., Zhang, W., Gu, Y., Huesges, Z., Chen, D., Liu, Y., Hao, L., Meng, S., Lu, Z., Li, S., & Luo, H. (2017). Crystal growth and phase diagram of 112-type iron pnictide superconductor $Ca_{1-y}La_yFe_{1-x}Ni_xAs_2$. *Superconductor Science and Technology*, *30*(9), 095002. https://doi.org/10.1088/1361-6668/aa7994

[27]: Bianconi, A. (2020, July 17). *Superconductivity in Quantum Complex matter: The superstripes landscape - journal of superconductivity and novel magnetism*. SpringerLink. Retrieved April 12, 2023, from https://link.springer.com/article/10.1007/s10948-020-05602-2

[28]: Martinelli, A., Bernardini, F., & Massidda, S. (2016). The phase diagrams of iron-based superconductors: Theory and experiments. *Comptes Rendus Physique*, *17*(1–2), 5–35. https://doi.org/10.1016/j.crhy.2015.06.001

[29]: Gu, Y., Liu, Z., Xie, T., Zhang, W., Gong, D., Hu, D., Ma, X., Li, C., Zhao, L., Lin, L., Xu, Z., Tan, G., Chen, G. F., Meng, Z. Y., Yang, Y., Luo, H., & Li, S. (2017). Unified Phase Diagram for Iron-Based Superconductors. *Physical Review Letters*, *119*(15). https://doi.org/10.1103/physrevlett.119.157001

[30]: Anderson, P. W. (1987). The Resonating Valence Bond State in La_2CuO_4 and Superconductivity. *Science*, *235*(4793), 1196–1198. https://doi.org/10.1126/science.235.4793.1196

[31]: Chubukov, A. V. (2012). Pairing Mechanism in Fe-Based Superconductors. *Annual Review of Condensed Matter Physics*, *3*(1), 57–92. https://doi.org/10.1146/annurev-conmatphys-020911-125055

[32]: Malaeb, W., Shimojima, T., Ishida, Y., Okazaki, K., Ota, Y., Ohgushi, K., Kihou, K., Saito, T., Lee, C. H., Ishida, S., Nakajima, M., Uchida, S., Fukazawa, H., Kohori, Y., Iyo, A., Eisaki, H., Chen, C.-T., Watanabe, S., Ikeda, H., & Shin, S. (2012). Abrupt change in the energy gap of superconducting ba. *Physical Review B*, *86*(16). https://doi.org/10.1103/physrevb.86.165117

[33]: Hardy, W. N., Bonn, D. A., Morgan, D. C., Liang, R., & Zhang, K. (1993). Precision measurements of the temperature dependence of λ in. *Physical Review Letters*, *70*(25), 3999–4002. https://doi.org/10.1103/physrevlett.70.3999

[34]: Tsuei, C. C., & Kirtley, J. R. (2002). D-wave pairing symmetry in cuprate superconductors—fundamental implications and potential applications. *Physica C: Superconductivity*, *367*(1-4), 1–8. https://doi.org/10.1016/s0921-4534(01)00976-5

[35]: Talantsev, E. F., Iida, K., Ohmura, T., Matsumoto, T., Crump, W. P., Strickland, N. M., Wimbush, S. C., & Ikuta, H. (2019). P-wave superconductivity in iron-based superconductors. *Scientific Reports*, *9*(1). https://doi.org/10.1038/s41598-019-50687-y

[36]: Chu, C.W., Deng, L.Z. & Wu, Z. The Retention and Study of High-Pressure-Induced Phases in High- and Room-Temperature Superconductors. *J Supercond Nov Magn* 35, 987–995 (2022). https://doi.org/10.1007/s10948-021-06117-0

[37]: Gupta, S. K. (2018). Review of high temperature superconductors and application in various fields. *Research & Development in Material Science*, *7*(4). https://doi.org/10.31031/rdms.2018.07.000668

[38]: Miccoli, I., Edler, F., Pfnür, H., & Tegenkamp, C. (2015). The 100th anniversary of the four-point probe technique: The role of probe geometries in isotropic and anisotropic systems. *Journal of Physics: Condensed Matter*, *27*(22), 223201. https://doi.org/10.1088/0953-8984/27/22/223201

[39]: Fujioka, M., Denholme, S. J., Ozaki, T., Okazaki, H., Deguchi, K., Demura, S., Hara, H., Watanabe, T., Takeya, H., Yamaguchi, T., Kumakura, H., & Takano, Y. (2013). Phase diagram and superconductivity at 58.1 K in α-FEAS-free smfeaso1−*x*F*x*. *Superconductor Science and Technology*, *26*(8), 085023. https://doi.org/10.1088/0953-2048/26/8/085023

[40]: Fagaly, R. (2006). Superconducting quantum interference device instruments and applications. *Review of Scientific Instruments*, *77*(10), 101101. https://doi.org/10.1063/1.2354545

[41]: *Squid magnetometer*. Quantum Design North America - Products - SQUID Magnetometer – Quantum Design MPMS®3. (n.d.). Retrieved April 12, 2023, from https://www.qdusa.com/products/mpms3.html